Atmos. Chem. Phys. Discuss., 15, 19947–20011, 2015
www.atmos-chem-phys-discuss.net/15/19947/2015/
doi:10.5194/acpd-15-19947-2015

Atmospheric Chemistry and Physics Discussions

Development of an atmospheric N_2O isotopocule model and optimization procedure, and application to source estimation

K. Ishijima[1], M. Takigawa[1], K. Sudo[2,1], S. Toyoda[3], N. Yoshida[4,5], T. Röckmann[6], J. Kaiser[7], S. Aoki[8], S. Morimoto[8], S. Sugawara[9], and T. Nakazawa[8]

[1]Department of Environmental Geochemical Cycle Research, JAMSTEC, Yokohama, Japan
[2]Graduate School of Environmental Studies, Nagoya University, Nagoya, Japan
[3]Department of Environmental Science and Technology, Tokyo Institute of Technology, Yokohama, Japan
[4]Department of Environmental Chemistry and Engineering, Tokyo Institute of Technology, Yokohama, Japan
[5]Earth-Life Science Institute, Tokyo Institute of Technology, Tokyo, Japan
[6]Institute for Marine and Atmospheric research Utrecht, Utrecht University, Utrecht, the Netherlands
[7]Centre for Ocean and Atmospheric Sciences, School of Environmental Sciences, University of East Anglia, Norwich, UK

[8]Center for Atmospheric and Oceanic Studies, Tohoku University, Sendai, Japan
[9]Miyagi University of Education, Sendai, Japan

Received: 31 May 2015 – Accepted: 29 June 2015 – Published: 22 July 2015

Correspondence to: K. Ishijima (ishijima@jamstec.go.jp)

Published by Copernicus Publications on behalf of the European Geosciences Union.

ACPD
15, 19947–20011, 2015

Abstract

This paper presents the development of an atmospheric N_2O isotopocule model based on a chemistry-coupled atmospheric general circulation model (ACTM). We also describe a simple method to optimize the model and present its use in estimating the isotopic signatures of surface sources at the hemispheric scale. Data obtained from ground-based observations, measurements of firn air, and balloon and aircraft flights were used to optimize the long-term trends, interhemispheric gradients, and photolytic fractionation, respectively, in the model. This optimization successfully reproduced realistic spatial and temporal variations of atmospheric N_2O isotopocules throughout the atmosphere from the surface to the stratosphere. The very small gradients associated with vertical profiles through the troposphere and the latitudinal and vertical distributions within each hemisphere were also reasonably simulated. The results of the isotopic characterization of the global total sources were generally consistent with previous one-box model estimates, indicating that the observed atmospheric trend is the dominant factor controlling the source isotopic signature. However, hemispheric estimates were different from those generated by a previous two-box model study, mainly due to the model accounting for the interhemispheric transport and latitudinal and vertical distributions of tropospheric N_2O isotopocules. Comparisons of time series of atmospheric N_2O isotopocule ratios between our model and observational data from several laboratories revealed the need for a more systematic and elaborate intercalibration of the standard scales used in N_2O isotopic measurements in order to capture a more complete and precise picture of the temporal and spatial variations in atmospheric N_2O isotopocule ratios. This study highlights the possibility that inverse estimation of surface N_2O fluxes, including the isotopic information as additional constraints, could be realized.

ACPD
15, 19947–20011, 2015

1 Introduction

Nitrous oxide (N_2O) is currently one of the most remarkable atmospheric components of the Earth's environment, being both a greenhouse gas with high radiative efficiency (100 year global warming potential or global temperature change potential of 200–300; Ciais et al., 2013), as well as the most influential ozone depleting substance (ODS) emitted during this century, when CFC emissions have been largely reduced following the Montreal Protocol (Ravishankara et al., 2009). N_2O was originally a natural gas component that was shown (from ice core records) to have existed prehistorically in the atmosphere (Schilt et al., 2010), and was mainly produced as an intermediate product or by-product during microbial utilization of nitrogen compounds in soils or oceans. Generated in this way on the Earth's surface, N_2O is chemically inert in the troposphere. However, in the stratosphere, N_2O is decomposed by photolysis and reaction with $O(^1D)$. The latter reaction is a source of nitric oxide (NO), which is a main player for stratospheric ozone depletion.

Around the mid-19th century, as industrialization expanded, the atmospheric N_2O mole fraction began to increase, and this growth was further accelerated in the 20th century (Machida et al., 1995; MacFarling Meure et al., 2006) following the increase in global population. This increase in N_2O levels is thought to have been caused by the use of synthetic nitrogen fertilizers developed during the industrialization of the agricultural sector. Through the application of nitrogen fertilizers onto crops, the amount of nitrogen compounds available for microbes increased, and N_2O production inevitably increased in the soil. It would be difficult to quickly reduce nitrogen fertilizer use in crop production (in order to reduce N_2O emissions) if we continue to feed the rapidly increasing global population. Thus, the increase in the atmospheric N_2O mole fraction has continued at a rate of around 0.5–0.8 $\mathrm{nmol\,mol^{-1}\,a^{-1}}$ near the surface since the 1980s (Ciais et al., 2013). Various N_2O sources other than agricultural soils are known, and the sum of their emissions (2.8 $\mathrm{Tg\,a^{-1}}$ N equivalents) is considered to be about 30 % less than agricultural soil emissions alone (4.1 $\mathrm{Tg\,a^{-1}}$ N), but the contri-

ACPD
15, 19947–20011, 2015

bution from each source to the global total is still only poorly understood and there are large uncertainties in the estimates (Ciais et al., 2013). Emission estimates for individual source categories are mainly derived from bottom-up approaches that combine field flux measurements and statistical data (e.g., data on nitrogen fertilizer use in a given region), but large spatiotemporal variations in the N_2O flux exist at the site to local scales. Consequently, it is difficult to make representative and accurate emission estimates for each source, and thus develop strategies to efficiently reduce N_2O emissions at global and national levels.

One approach to separating out the contributions from individual sources is the use of isotopically-substituted molecules, or, short, isotopocules (Kaiser and Röckmann, 2008). The isotopocule ratio of N_2O is altered by various biogeochemical processes, such as biogenic production and consumption in the source areas, and also by chemical processes in the atmosphere. The isotopic composition of the precursors is also reflected to some degree in the resultant N_2O. Therefore, it is thought that stable isotopocule ratios could be used to quantify the contribution from individual N_2O sources. There have been many studies of the isotopic signatures of various N_2O sources and sinks, but a unique isotopic value for each source with an adequately small uncertainty range remains elusive because of the complicated tangle of the precursor's isotopic signatures and microbial process-driven isotopic fractionation (e.g., Kim and Craig, 1993; Rahn and Wahlen, 2000; Toyoda et al., 2011, 2015). There have also been experimental or theoretical studies of isotopic fractionation driven by photochemical loss reactions (e.g., Selwyn and Johnston, 1981; Kaiser et al., 2002, 2003a; Nanbu and Johnson, 2004; von Hessberg et al., 2004; Schmidt et al., 2011). This fractionation generates large vertical gradients in N_2O mole fraction and isotopocule ratios, which decrease and increase, respectively, with increasing altitude in the stratosphere (e.g., Kim and Craig, 1993; Park et al., 2004; Toyoda et al., 2004; Kaiser et al., 2006). For the troposphere, and based on ice core analysis, firn air analysis, or direct atmospheric measurements, long-term trends have been mainly studied for the period from the mid-1700s to the present (Sowers et al., 2002; Röckmann et al., 2003; Röckmann and

ACPD
15, 19947–20011, 2015

Levin, 2005; Bernard et al., 2006; Ishijima et al., 2007), although some recent studies have discussed seasonal cycles or interhemispheric differences (Park et al., 2012; Toyoda et al., 2013). These studies have revealed that the observed decreasing trends of, for example, the major nitrogen and oxygen isotope ratios of N_2O, are caused by the continuous input of N_2O into the troposphere from anthropogenic sources, which, based on a top-down approach using a simple box model and observed data, are estimated to be on average isotopically lighter than tropospheric N_2O (Toyoda et al., 2015).

It is now necessary to progress to the next stage of integrating the knowledge obtained (as above), and to comprehensively validate this knowledge, in order to reconsider how and what should be the focus of study in this field. Global three-dimensional (3-D) modelling is considered a possible avenue for such research. There have already been some attempts at global N_2O isotopocule modelling (McLinden et al., 2003; Morgan et al., 2004; Liang and Yung, 2007), but existing models have a fixed N_2O mole fraction in the lower troposphere and no surface emissions, or are sometimes two-dimensional, and this is because they were developed mainly to examine photochemistry-induced isotopocule fractionation in the stratosphere. On the other hand, several studies have performed global N_2O inverse modelling to estimate regional fluxes (Hirsch et al., 2006; Huang et al., 2008; Thompson et al., 2014a; Saikawa et al., 2014). The derived regional N_2O emission estimates are generally reasonable, predominantly because of recently improved observation networks incorporating flask sampling and in situ measurements (e.g., Dlugokencky et al., 1994; Tohjima et al., 2000; Prinn et al., 2000; Ishijima et al., 2009). However, it is still thought that some of the uncertainty in inverse estimations is caused by poor simulation of the stratosphere–troposphere exchange (STE), which brings stratospheric N_2O-depleted air into the troposphere and influences spatiotemporal variations in the tropospheric mole fraction. In terms of isotopocules, the N_2O thus introduced into the troposphere by STE is rich in heavier isotopocules, as N_2O is enriched in heavier isotopocules in the stratosphere by photochemical loss processes; therefore, as discussed by Park et al. (2012), isotopocules can be used to estimate the effect of STE on tropospheric N_2O mole frac-

ACPD
15, 19947–20011, 2015

tions. Unfortunately, atmospheric N_2O isotopocule measurements have not reached the level required for such inverse modelling or STE studies in terms of measurement precision and number of stations. However, in the near future, when high-frequency and high-precision optical measurement systems capable of continuously monitoring atmospheric N_2O isotopocule ratios (e.g., Waechter et al., 2008) are improved and become more widely available, global atmospheric N_2O isotopocule models could be essential to our understanding of observed results (e.g., see Rigby et al., 2012 for the case of methane). Therefore, in this study we present an outline of a newly developed N_2O isotopocule model that explicitly handles surface emissions, together with a simple approach to optimizing the model's photochemical fractionation and surface emissions using several types of observational data.

2 N_2O isotopocules

2.1 Notation for N_2O isotopocules

In this study, we use the term "isotopocule", which was first proposed by Kaiser and Röckmann (2008) and has also recently been adopted by Coplen (2011) to designate isotopically substituted molecules. The term encompasses the terms "isotopologue" (a molecule differing only in isotopic composition; e.g., $^{14}N^{14}N^{16}O$ and $^{14}N^{14}N^{18}O$) and "isotopomer" (molecules having the same number of each isotopic atom but differing in their positions; e.g., $^{14}N^{15}N^{16}O$ and $^{15}N^{14}N^{16}O$). Individual N_2O isotopocules are distinguished by their molecular formula. We consider the following four N_2O isotopocules: $^{14}N^{14}N^{16}O$, $^{14}N^{15}N^{16}O$, $^{15}N^{14}N^{16}O$, and $^{14}N^{14}N^{18}O$ in this study, and the notation of the isotopocule ratios is as follows (Toyoda and Yoshida, 1999):

ACPD
15, 19947–20011, 2015

$$\delta^{15}N^{i} = {}^{15}R^{i}_{sample} / {}^{15}R^{i}_{std} - 1, \quad (i = \text{bulk}, \alpha \text{ or } \beta) \tag{1}$$

$$\delta^{18}O = {}^{18}R_{sample} / {}^{18}R_{std} - 1, \tag{2}$$

$${}^{15}R^{\alpha} = \left[{}^{14}N^{15}N^{16}O\right] / \left[{}^{14}N^{14}N^{16}O\right], \tag{3}$$

$${}^{15}R^{\beta} = \left[{}^{15}N^{14}N^{16}O\right] / \left[{}^{14}N^{14}N^{16}O\right], \tag{4}$$

$${}^{15}R^{bulk} = \left({}^{15}R^{\alpha} + {}^{15}R^{\beta}\right)/2, \tag{5}$$

$${}^{18}R = \left[{}^{14}N^{14}N^{18}O\right] / \left[{}^{14}N^{14}N^{16}O\right]. \tag{6}$$

We also use the ^{15}N site preference (hereafter $\delta^{15}N^{sp}$), which is defined as the difference between the two nitrogen isotopomer deltas:

$$\delta^{15}N^{sp} = \delta^{15}N^{\alpha} - \delta^{15}N^{\beta}. \tag{7}$$

We note that in some publications, a different notation for the N_2O isotopomers was used, following Brenninkmeijer and Röckmann (1999). In publications from this group, $\delta^{15}N^{\alpha}$ is denoted ${}^{2}\delta^{15}N$ and $\delta^{15}N^{\beta}$ is denoted ${}^{1}\delta^{15}N$. Hereafter, we use "isotopocule deltas" as an inclusive term for $\delta^{15}N^{bulk}$, $\delta^{18}O$, $\delta^{15}N^{\alpha}$, $\delta^{15}N^{\beta}$, and $\delta^{15}N^{sp}$.

2.2 Conversion of isotopocule ratio to mole fraction

When we simulate N_2O isotopocules in a model or use the observational data to optimize the model, the isotopocule ratios must be converted to the absolute mole fractions. In this study, we calculated each isotopocule mole fraction assuming that N_2O consists of only four isotopocules: $^{14}N^{14}N^{16}O$, $^{14}N^{15}N^{16}O$, $^{15}N^{14}N^{16}O$, and $^{14}N^{14}N^{18}O$ as follows:

$$\left[N_2O\right] = \left[{}^{14}N^{14}N^{16}O\right] + \left[{}^{14}N^{15}N^{16}O\right] + \left[{}^{15}N^{14}N^{16}O\right] + \left[{}^{14}N^{14}N^{18}O\right]. \tag{8}$$

By substituting Eqs. (3), (4), and (6) into Eq. (8), we have

$$\left[{}^{14}N^{14}N^{16}O\right] = \left[N_2O\right] / \left(1 + {}^{15}R^{\alpha} + {}^{15}R^{\beta} + {}^{18}R\right). \tag{9}$$

ACPD
15, 19947–20011, 2015

As these four isotopocules account for more than 99.9 % of all of the atmospheric N_2O isotopocules, and assuming statistical isotope distributions for the three atoms in the N_2O molecule ($x(^{14}N^{14}N^{16}O)$ = 99.01 %, $x(^{14}N^{15}N^{16}O)$ = 0.37 %, $x(^{15}N^{14}N^{16}O)$ = 0.36 %, and $x(^{14}N^{14}N^{18}O)$ = 0.21 %), neglecting less abundant species, will not generate any significant errors in the N_2O isotopocule ratios finally obtained.

3 Observational data

We used three sets of observation data in the model optimization and analysis in this study. Table 1 and Fig. 1 summarize the details of the ground-based stations and the locations of all observations, respectively.

3.1 Time series data observed at a ground-based station

We used the high-precision N_2O isotopocule ratio measurements of Röckmann and Levin (2005). Air sampling was performed at the German Antarctic research station Neumayer (71° S, 8° W, hereafter NMY) by the Alfred Wegener Institute for Polar Research (AWI, Bremerhaven) since the early 1980s. From this dataset, twenty-three archived air samples for the period from March 1990 to November 2002 were analysed for N_2O mole fraction at the University of Heidelberg (Schmidt et al., 2001) using ECD-GC (an Electoron Capture Detector equipped Gas Chromatography), based on a standard scale developed by The Advanced Global Atmospheric Gases Experiment (AGAGE), and also a high-precision isotopocule ratio measurement technique (Röckmann et al., 2005) for isotopocule ratios at the Max Planck Institute for Nuclear Physics (Heidelberg). This dataset shows highly stable temporal variations (standard error about 0.14 nmol mol^{-1}, 0.01, 0.02, 0.07, and 0.06 ‰ for the mole fraction, $\delta^{15}N^{bulk}$, $\delta^{18}O$, $\delta^{15}N^{\alpha}$, and $\delta^{15}N^{\beta}$, respectively) compared with other datasets (Park et al., 2012; Toyoda et al., 2013), because the measurement precision was very high, and also the station is very close to being a true background site and so is less af-

ACPD
15, 19947–20011, 2015

fected by nearby sources. The advantage is obvious in comparison with other stations showing highly variable results and sometimes blurring the trends due to low measurement precisions and/or local source influences (Fig. 10). Consequently, this dataset was considered suitable for the first step of developing an N_2O isotopocule model with simplified surface emissions of a spatiotemporally constant isotopocule ratio. In Röckmann and Levin (2005), results for $\delta^{15}N^{\alpha}$ and $\delta^{15}N^{\beta}$ are shown using two different standard scales from the Max-Planck Institute (Kaiser et al., 2003b) and the Tokyo Institute of Technology (Toyoda and Yoshida, 1999), but we used the latter scale, which has been supported by further reports (Griffith et al., 2009; Westley et al., 2007), for all data in this study.

3.2 Time series data reconstructed from analysis of firn air obtained from the polar ice sheets

We also used historical data of atmospheric N_2O mole fraction and isotopocule ratios, which were reconstructed from analysis of firn air samples obtained from three stations in both the Arctic and Antarctic regions (Ishijima et al., 2007; Table 1; Fig. 1); North GRIP (75° N, 43° W, 2959 m a.s.l., hereafter NGR), Greenland, Dome Fuji (77° S, 40° E, 3810 m a.s.l., hereafter DFJ) and H72 (69° S, 41° E, 1241 m a.s.l.), Antarctica. Measurement precision (N_2O: 0.3 nmol mol^{-1}; $\delta^{15}N^{bulk}$: 0.1 ‰; $\delta^{18}O$: 0.2 ‰) was not as high as the data from NMY, but only the decadal means of the record, which improves the standard error of the data, were used to limit the uncertainty in this study. The standard scale was not adjusted to derive the interhemispheric differences, because all firn air samples were measured using a single analytical system with the same standard scale. Thus, we can ignore uncertainties caused by the standard scale difference, and it is a great advantage of this dataset.

ACPD
15, 19947–20011, 2015

3.3 Vertical profile data in the stratosphere observed using balloon and aircraft

To validate the model for N_2O mole fraction and isotopocule ratios in the stratosphere, we used vertical profile data observed by balloons and aircraft between 1987 and 2007 (Toyoda et al., 2004; Kaiser et al., 2006). Toyoda et al. (2004) published balloon observation data obtained until 2001, but unpublished data obtained by these authors between 2002 and 2007 were also included in this study. Balloons were launched over locations in Sweden, France, India, Japan, and Antarctica (Fig. 1; detailed observation information in Toyoda et al., 2004; Kaiser et al., 2006), and 6 to 15 air samples were collected during each flight using a cryogenic sampler on board the balloon at altitudes of 10–35 km. Some aircraft observations from up to around 20 km height (Kaiser et al., 2006), were also used in this study. Air samples were analysed for N_2O mole fraction and isotopic composition in the laboratory. Measurement precisions ($N_2O < 1\,\%$; $\delta^{15}N^{bulk}$ and $\delta^{18}O \cong 0.5\,‰$; $\delta^{15}N^{\alpha}$ and $\delta^{15}N^{\beta} < 1.5\,‰$) of the stratospheric samples were relatively poor because of the limited volume of air sample taken, especially from higher altitudes, but were considered to be adequate considering the large vertical gradients in the stratosphere.

4 Modelling

4.1 Model outline

We used the Center for Climate System Research/National Institute for Environmental Stu-dies/Frontier Research Center for Global Change atmospheric general circulation model (CCSR/NIES/FRCGC AGCM; Numaguti et al., 1997) with chemical reactions (which we refer to as the ACTM) to simulate atmospheric N_2O isotopocules. This model was described by Ishijima et al. (2010), but some improvements were made to the chemistry–radiation calculations to better reproduce the stratospheric N_2O isotopocules (described below). The horizontal and vertical resolutions of the model

ACPD
15, 19947–20011, 2015

were T42 spectral truncation (about 2.8° × 2.8°) and 67 sigma-pressure vertical layers (surface to about 80 km), respectively. The model transport was nudged towards the Japanese 25 year ReAnalysis data by the Japan Meteorological Agency (JMA) (JRA-25; Onogi et al., 2007) for horizontal winds and temperature at 6 hly time intervals.

4.1.1 Stratospheric chemistry

The chemical loss of N_2O by photolysis and two different oxidation reactions with $O(^1D)$ in the stratosphere were incorporated into the model. Absorption cross-sections of N_2O and the oxidation reaction rate constants, which depend on the ultraviolet wavelength and/or the air temperature, were taken from Sander et al. (2006). The N_2O photolysis rate (J_{N_2O}) was calculated for 15 bins from 178 to 200 nm (Schumann–Runge bands) by a scheme (Akiyoshi et al., 2009) using the parameterization of Minschwaner et al. (1993), and for 3 bins from 200 to 278 nm by a main radiation–photolysis scheme of the ACTM (Sudo et al., 2002; Sekiguchi and Nakajima, 2008). The concentration of $O(^1D)$ was calculated online in the ACTM using the prescribed ozone field, and the photolysis of ozone was calculated for 9 bins from 200 to 355 nm. For the ozone field, 6 hly full-resolution model level data from the ECMWF Interim Reanalysis (ERA-Interim, Dragani, 2011), and from Takigawa et al. (1999), were used up to and above 1 hPa, respectively.

4.1.2 Isotopocule fractionation

N_2O isotopocule fractionation driven by photochemical reactions was incorporated into the ACTM. We used the photolytic fractionation constants for $^{14}N^{15}N^{16}O$ and $^{15}N^{14}N^{16}O$ of von Hessberg et al. (2004), which depend on both wavelength and air temperature. We approximated the constant for $^{14}N^{14}N^{18}O$, as it was not determined by von Hessberg et al. (2004). We first calculated apparent fractionation constants (hereafter εs), which are the slopes of the lines fitted to the Rayleigh plot of the stratospheric data, of $\delta^{18}O$, $\delta^{15}N^{\alpha}$, and $\delta^{15}N^{\beta}$ for the balloon observation data of Toy-

ACPD
15, 19947–20011, 2015

oda et al. (2004), and then interpolated the constants for $^{14}N^{15}N^{16}O$ and $^{15}N^{14}N^{16}O$ to obtain that of $^{14}N^{14}N^{18}O$ so that the relationship of the εs of $\delta^{15}N^{\alpha}$, $\delta^{15}N^{\beta}$, and $\delta^{18}O$ was the same as that of the fractionation constants of $^{14}N^{15}N^{16}O$, $^{15}N^{14}N^{16}O$, and $^{14}N^{14}N^{18}O$. However, these photolytic fractionations implemented in the model were found to underestimate the observed εs, so we slightly modified the fractionation in the model using a simple optimization method, as described in Sect. 4.2.3. For oxidation with $O(^1D)$, we used the mean fractionation constants determined by Kaiser et al. (2002), but we did not consider temperature dependence of the fractionations, which are very small and thus do not contribute strongly to the fractionations in the stratosphere compared to the photolytic fractionations. The four different species, $^{14}N^{14}N^{16}O$, $^{14}N^{15}N^{16}O$, $^{15}N^{14}N^{16}O$, and $^{14}N^{14}N^{18}O$, are calculated separately in the model.

4.1.3 Emission scenarios

We included the four source categories of N_2O emissions in the model simulations in this study; i.e., natural soils, oceans, anthropogenic, and biomass burning emissions. The annual mean natural soil emissions of N_2O were taken from the Emission Database for Global Atmospheric Research version 2 (EDGARv2; http://themasites.pbl.nl/tridion/en/themasites/edgar/emission_data/edgar2-1990). For oceanic emissions, the monthly varying emissions provided by Bouwman et al. (1995) (mostly based on Nevison et al., 1995) and Jin and Gruber (2003) were combined, but scaled by 0.45 and 0.55, respectively. For anthropogenic emissions, we used the annual mean emissions from EDGARv4.2 (covering 1970–2000; http://edgar.jrc.ec.europa.eu) for 1984–1999, and from EDGARv4.2 FT2010 (covering 2000–2010) for 2000–2010, but the emissions from EDGARv4.2 were scaled so that the global total emissions of each source category were consistent in 2000 between EDGARv4.2 and EDGARv4.2 FT2010. The anthropogenic emissions for 2011 were kept the same as those in 2010. For emissions from biomass burning, we used the monthly varying

ACPD
15, 19947–20011, 2015

emissions from the REanalysis of the TROpospheric chemical composition over the past 40 years (RETRO, covering 1960–2000; Schultz et al., 2008) for the period 1984–1996, and from the Global Fire Emissions Database (GFED3.1, covering 1997–2011; van der Werf et al., 2010) for 1997–2011, but emissions of RETRO were scaled so that the global total emissions were consistent in 1997 between RETRO and GFED3.1.

This base emission scenario was multiplied by a single scaling factor that was homogeneous in space and time, and used for the simulations of each N_2O isotopocule. The model was optimized for both the long-term trends and north-to-south gradients of tropospheric N_2O isotopocules using the observed data. For the long-term trend optimization, we prepared small and large emission scenarios for each isotopocule by scaling as mentioned above. The scaling factors and mean annual total emissions for the period 1991–2001 are shown in Table 2, and temporal changes in the emissions are shown in Fig. S1 in the Supplement. To optimize the north-to-south gradients, we additionally scaled the emissions using different factors for both hemispheres, but evenly within each hemisphere. The scaling factors were selected so that the average ratio of Northern Hemispheric emissions (E_{NH}) to Southern Hemispheric emissions (E_{SH}) for the period 1991–2001 became 0.8 and 1.3 times the ratio of the base emission scenario for small and large $E_{NH} : E_{SH}$ ratio cases, respectively. By this operation, the $E_{NH} : E_{SH}$ ratio of the base emission scenario of about 1.5 became about 1.2 and 2.0 for the small and large emissions scenarios, respectively. The horizontal and latitudinal distributions of these emissions are shown in Fig. S1. We regard this range (1.2–2.0) as sufficient, based on our model's hemispheric transport feature in previous N_2O modelling studies, in which the ACTM could well reproduce the north-to-south gradients of the atmospheric N_2O mole fraction with the range of the $E_{NH} : E_{SH}$ ratio from 1.3 to 1.9 (Ishijima et al., 2010; Thompson et al., 2014b, c). Finally, we prepared four different emission scenarios for each N_2O isotopocule: small and large global total emissions, and small and large $E_{NH} : E_{SH}$ ratios.

ACPD
15, 19947–20011, 2015

4.1.4 Model run and initial field

We ran the model for the period 1984–2011 starting with well spun-up initial distributions of atmospheric N_2O isotopocule mole fractions. The 3-D initial mole fraction field was obtained from a spin-up run with a "semi-equilibrium state" for a total of more than 50 years. "Semi- equilibrium state" here means that the atmospheric N_2O trend was mostly maintained at realistic levels, the vertical profile in the stratosphere being also realistic, by balancing the increasing surface emissions with the stratospheric loss. Spin-up is important to simulate atmospheric N_2O and to precisely estimate surface emissions of N_2O isotopocules by comparing the model and observation data, because the lifetime of N_2O is very long (~ 120 years). As for the emissions, the initial mole fraction field was also scaled to prepare small and large initial value cases for the model optimization so that the mole fractions near the surface roughly covered the range of observed mole fractions for each isotopocule (Table 2).

4.2 Model optimization

In this study, we optimized the N_2O isotopocule model for global total emissions (using the atmospheric long-term trend), the ratio of Northern Hemisphere to Southern Hemisphere emissions (using the atmospheric north–south gradient), and photolytic isotopocule fractionation (using the vertical gradient in the stratosphere) of each isotopocule. To accomplish this, we ran the model with several different simulation scenarios for each isotopocule, and then, after multiplied by scaling factors, combined the results so that the combined results were as close as possible to the measurements. In this section, we explain the optimization procedures; the workflow is shown in Fig. 2.

ACPD
15, 19947–20011, 2015

4.2.1 Model optimization for tropospheric long-term trend and global total emissions

To optimize the model, we confirmed that the model system was linear for some points throughout the atmosphere from the surface to the stratosphere in the N_2O simulation, as follows:

$$S(P_3) = fS(P_1) + (1-f)S(P_2), \quad (10a)$$

$$P_3 = fP_1 + (1-f)P_2. \quad (10b)$$

Here, P is one of the parameters in the model related to atmospheric N_2O isotopocule simulation, either the initial value of the atmospheric N_2O isotopocule mole fraction (I), global total emissions (E), the Northern Hemisphere to Southern Hemisphere emission ratio (e), or the photolytic fractionation (J). Subscript numbers are used for the same parameter but the values are different. In Eq. (10a), $S(P_1)$, $S(P_2)$, and $S(P_3)$ are the results of an atmospheric N_2O isotopocule from the simulations, in which only the parameter P differed among the three simulations and the other parameters remained the same. f is a scaling factor, generally ranging from 0 to 1. For example, assume that there were two model simulations, in which only the global N_2O emissions are different being 14 and 17 $\mathrm{Tg\,a^{-1}\,N}$ (E_1 and E_2), respectively. They show 300 and 310 $\mathrm{nmol\,mol^{-1}}$ ($S(E_1)$ and $S(E_2)$) at a particular location, date and time, respectively. If other simulation, in which only the global emission is different from the above two simulations, shows 303 $\mathrm{nmol\,mol^{-1}}$ ($S(E_3)$), it is true according to Eqs. (10a) and (10b) that $f = 0.7$ and $E_3 = fE_1 + (1-f)E_2 = 14.9\,\mathrm{Tg\,a^{-1}\,N}$, because $303 = 0.7 \times 300 + (1-0.7) \times 310 (S(E_3) = f \times S(E_1) + (1-f) \times S(E_2))$. Theoretically, if the model results are indeed linear for several parameters, Eqs. (10a) and (10b) are also valid for multiple parameters as follows:

ACPD
15, 19947–20011, 2015

$$S(I_1, E_3) = f_E S(I_1, E_1) + (1 - f_E) S(I_1, E_2), \quad (11a)$$

$$S(I_2, E_3) = f_E S(I_2, E_1) + (1 - f_E) S(I_2, E_2), \quad (11b)$$

$$E_3 = f_E E_1 + (1 - f_E) E_2, \quad (11c)$$

$$S(I_3, E_3) = f_I S(I_1, E_3) + (1 - f_I) S(I_2, E_3), \quad (11d)$$

$$I_3 = f_I I_1 + (1 - f_I) I_2. \quad (11e)$$

Here, $S(I_3, E_3)$ is the result of a simulation using I_3 and E_3, but can actually be produced by combining four different simulation results: $S(I_1, E_1)$, $S(I_1, E_2)$, $S(I_2, E_1)$, and $S(I_2, E_2)$, and the scaling factors f_E and f_I. Thus, using these four simulation results, we can determine the optimum values of I and E by assigning optimal values to f_E and f_I such that the result $S(I_3, E_3)$ best fits the observations (Figs. 2 and 3). More simply, we optimize the "f" values so that combinations of the four model simulation results using the "f" values fit the observed results in a least square sense. Finally, we can write as follows:

$$\text{Observation} \cong S(I_3, E_3) \quad (11f)$$

$$E_{\text{opt}} = E_3 \quad (11g)$$

$$I_{\text{opt}} = I_3 \quad (11h)$$

Here, E_{opt} and I_{opt} are optimized E and I, respectively. The least square approach is explained later in this section.

It is known that time series of atmospheric N_2O mole fractions and isotopocule ratios near the surface have almost linear trends over a decadal timescale, so the budget equation for each isotopocule i can be written as follows:

$$dM_i/dt = E_i - k_i M_i, \quad (12a)$$

$$M_i = M_{i0} + \int \{E_i - k_i M_i\} dt, \quad (12b)$$

ACPD
15, 19947–20011, 2015

where M_i is the global total mass of an N_2O isotopocule i (Tg), E_i is the total emission (Tg a^{-1}), k_i is the mass-weighted global mean chemical loss rate coefficient (a^{-1}), and M_{i0} is the initial mass (Tg). As N_2O is fairly well mixed in the troposphere, M_i and M_{i0} can be substituted by F_iC_i and F_iC_{i0} over a decadal timescale, where C_i is the atmospheric mole fraction of each N_2O isotopocule i (nmol mol^{-1}) at a station and F_i is a conversion factor from mole fraction (nmol mol^{-1}) to mass (Tg), generally around 4.8 Tg per nmol mol^{-1} for $^{14}N^{14}N^{16}O$ (F_1), as follows:

$$dC_i/dt = E_i/F_i - k_iC_i, \tag{13a}$$

$$C_i = C_{i0} + \int \{E_i/F_i - k_iC_i\}dt. \tag{13b}$$

In Eq. (13a), the growth rate depends on the surface emission E_i and atmospheric loss k_iC_i. In our simulations, as the loss rate coefficient k_i is prescribed by the model meteorology, which is driven by reanalysis data and short- and long-wave radiation produced by the prescribed fields of greenhouse gases and ozone etc., C_i itself, as well as E_i, determine the atmospheric trend dC_i/dt. Furthermore, Eq. (13b) indicates that C_i also depends on the initial value C_{i0}. This means that the model can produce any decadal trend of atmospheric N_2O, and certainly the observed trend, if appropriate values of C_{i0} and E_i are used. However, if the spin-up is insufficient, surface emission estimated by Eq. (13b) becomes invalid, as mentioned in Sect. 4.1.4. Thus, in this study we optimized the model for long-term trends of atmospheric N_2O isotopocules to reproduce the results observed at NMY, by using Eqs. (11a)–(11e) and determining optimal values of f_E and f_I. By this process, surface emissions and initial values were also optimized as shown in Eqs. (11c) and (11e). In the actual optimizations, for all terms in Eqs. (11a)–(11e), the subscript numbers 1, 2, and 3 are substituted by small, large, and optimized, respectively.

A combination of optimal values of f_E and f_I was identified for each isotopocule so that $\sum_i (C_{\mathrm{model}_i} - C_{\mathrm{observation}_i})^2$ (C_{XXX_i}: mole fraction for observation or model at each data point i) was minimized (Figs. 2 and 3). In case of the f values being out of 0 to 1,

ACPD
15, 19947–20011, 2015

the initial ranges for searching the optimal f values were set to a relatively wide range of −1 to 2. The optimal f values were searched by sequentially changing the values, the intervals and ranges being gradually reduced. In the actual calculation, the first guess of the combination ($f_{E,1}$ and $f_{I,1}$) was obtained with an accuracy of 0.3 in the range of −1 to 2, the second guess ($f_{E,2}$ and $f_{I,2}$) with an accuracy of 0.15 in the ranges of $f_{E,1} \pm 0.75$ and $f_{I,1} \pm 0.75$, the third guess ($f_{E,3}$ and $f_{I,3}$) with an accuracy of 0.075 in the ranges of $f_{E,2} \pm 0.375$ and $f_{I,2} \pm 0.375$, and the final results were obtained with an accuracy better than 10^{-10}. All results for the f values eventually became between 0 and 1. The uncertainty caused by the optimization method was estimated using a Monte Carlo approach for the f values, by assigning random errors to the observational data 100 000 times. The random errors were taken from a Gaussian distribution representing the measurement standard error. Uncertainty in the surface emissions was also simultaneously estimated using Eq. (11c). Further details of this optimization procedure are provided in the Supplement.

4.2.2 Model optimization for tropospheric north-to-south gradient and the Northern Hemisphere to Southern Hemisphere emission ratio

The Northern Hemisphere to Southern Hemisphere emission ratio (e) was optimized in almost the same manner as the long-term trend, but more simply (Fig. 2). Time series data, reconstructed from analysis of firn air samples obtained from polar ice sheets (Table 1; Sect. 3.2) were used for this. As shown in Fig. 2, this optimization was performed after the model had been optimized for the long-term trend, because the emission ratio optimization has greater freedom with respect to the f values because of the use of only the interpolar difference (not the absolute value) and the relatively large measurement error compared to the signal. As described in Sect. 4.1.3, we prepared two different emission scenarios with small and large emission ratios for each isotopocule, and optimized e as follows:

ACPD
15, 19947–20011, 2015

$$S(e_{\mathrm{opt}}) = f_e S(e_{\mathrm{S}}) + (1 - f_e) S(e_{\mathrm{L}}), \quad (14a)$$

$$e_{\mathrm{opt}} = f_e e_{\mathrm{S}} + (1 - f_e) e_{\mathrm{L}}, \quad (14b)$$

where e_{S}, e_{L}, and e_{opt} are emission scenarios with small, large, and optimized emission ratios, respectively. As constrained by the observation data, the interhemispheric differences rather than the raw values of the time series from the firn air analysis were used. The time series was fitted using a spline curve and averaged over the period 1991–1998, and then the value of NGR, after subtracting the mean of the values of DFJ and H72, was used for optimization, because model values in the Southern Hemisphere are already optimized to fit the NMY data, and its standard scales differ from those for the firn data. The corresponding values are shown in Table 3. More details of this optimization are described in the Supplement.

There is no site preference information ($\delta^{15}N^{\alpha}$ and $\delta^{15}N^{\beta}$, or $\delta^{15}N^{\mathrm{sp}}$) available from the firn data of Ishijima et al. (2007), and no data on the interhemispheric difference of site preference have been published to date. To optimize the north–south gradients by our method, we need to assume a certain value for the $\delta^{15}N^{\mathrm{sp}}$ gradient. Therefore, we set the value and its uncertainty so that the estimated $\delta^{15}N^{\mathrm{sp}}$ value and its uncertainty range for each hemisphere's total sources did not exceed the range of the $\delta^{15}N^{\mathrm{sp}}$ values for various sources quoted in previous studies (see Fig. 9 in Toyoda et al., 2015). Following sensitivity tests, we concluded that no interpolar difference of $\delta^{15}N^{\mathrm{sp}}$ was the most reasonable choice (Table 3), which is the same as that assumed in Toyoda et al. (2013). However, as this value is set just for the optimization calculation, we will not discuss hemispheric $\delta^{15}N^{\mathrm{sp}}$ values any further in this study.

4.2.3 Tuning of photolytic fractionation

Based on some preliminary test simulations, which indicated that the initial photolytic fractionation values given to the model were slightly underestimated, we decided to simply tune the photolytic fractionation in the model. This was achieved by comparing

ACPD
15, 19947–20011, 2015

εs derived from Rayleigh plots of observation and model results in the stratosphere. As described above, the model was first optimized for long-term trends and north–south gradients in the troposphere, but actually the optimizations were completed for two independent model simulations, in which only photolytic fractionation was different. Then, the best fit to observed εs were obtained by interpolating the two simulation results.

The ε is often used as one of the indices for diagnosing the degree of isotopocule fractionation caused by photochemical reactions in the stratosphere (e.g., Toyoda et al., 2004; Kaiser et al., 2006). In this study, it was defined as the slope of linear fitting to the Rayleigh plot of the isotopocule data, following the definition by Toyoda et al. (2004; referred to as "isotopomer enrichment factors" therein). In the Rayleigh plot, $\ln\{(\delta+1)/(\delta_0+1)\}$ is plotted against $\ln\{[N_2O]/[N_2O]_0\}$. Here, δ and $[N_2O]$ are the relative isotopocule ratio difference and N_2O mole fraction, respectively, and those without and with the subscript 0 indicate the values in the stratosphere and of the origin, respectively. The origin ($[N_2O]_0$) is tropospheric N_2O, which has not yet suffered from photochemical loss. The air mass in the stratosphere is older than that in the troposphere, because it takes time for the tropospheric air to reach the middle to upper part of the stratosphere. The age of the air in the stratosphere is known to range from near zero to more than five years, depending on the altitude, latitude, and season; in the case of the air at the surface this was set to an age of zero years. Therefore, the N_2O mole fraction and isotopocule ratios of the origin for the air in the stratosphere are supposed to be those of the air in the troposphere in the past. In this study, we used the age of air calculated in the model to determine the values for the original air in the troposphere in the past. The N_2O mole fraction and isotopocule ratios observed at NMY, extrapolated back in time by linear fit, were used as the origin values. Actually, it is difficult to precisely determine the past values, as there are no high-precision measurement data available before 1990, but we regard the error of around 1 ‰ in the εs as acceptable for these calculations, considering the large vertical gradients in the stratosphere. In addition, as discussed by Ishijima et al. (2010), the ACTM tends to un-

ACPD
15, 19947–20011, 2015

derestimate the age in the stratosphere. However, even if the age differs by a maximum of two years between model and observation, the ε value does not change significantly, as temporal changes in the N_2O mole fraction and isotopocule ratios in the troposphere are quite small compared with the vertical gradients in the stratosphere.

The underestimation of the ε in the model might come from underestimation of the isotopocule fractionation caused by reaction with $O(^1D)$ in the model. However, the absolute value of the experimentally determined fractionation constant for photolysis (von Hessberg et al., 2004) are larger by about one order of magnitude compared to those for the $O(^1D)$ reaction (Kaiser et al., 2002). Overestimation of N_2O loss by the $O(^1D)$ reaction may lead to underestimation of the fractionation in the stratosphere by relative increase of the reaction with small isotopic fractionation. Lastly, excessive mixing and transport rates may also cause the apparent stratospheric fractionation to be too small (Kaiser et al., 2006).

We considered that the actual cause for the deficiencies of the stratospheric model simulations was not so important in this study focusing on the tropospheric N_2O, as long as vertical profiles of N_2O mole fraction and isotopocule ratios and apparent isotopic fractionation ε in the stratosphere were realistic. Therefore, we "corrected" the stratospheric model by artificially enhancing the photolysis isotope fractionation. To cover the range of observed ε values by model, photolysis rates of $^{14}N^{15}N^{16}O$, $^{15}N^{14}N^{16}O$, and $^{14}N^{14}N^{18}O$ were scaled by a factor of 0.985 (1.5 % reduced photolysis for the heavy isotopocules, leading to larger fractionation). This scaling leads to an increase of the fractionation constants by about 14 ‰, outside the uncertainty of the experimental results of von Hessberg et al. (2004; Figs. 3a, b and 4a, b) of about 2 ‰ (1σ) in the stratospherically relevant wavelength range.

Another motivation for adjusting the photolysis rates in the model, as described in Sect. 4.1.1, was that the wavelength resolution of the photolysis calculation in the ACTM was coarse, being only parameterized below 200 nm by a simple scheme, and separated into only three bins above 200 nm, whereas the photolysis of ozone, which is important for the production of $O(^1D)$ in the stratosphere, was calculated in nine wave-

ACPD
15, 19947–20011, 2015

length bins. The coarse wavelength resolution could lead to the uncertainty of N_2O isotopocule fractionations calculated in the ACTM, and the adjustment should take this into account.

The mean ε for all balloon and aircraft observations in the stratosphere (Toyoda et al., 2004; Kaiser et al., 2006), which is the slope of the linear fit to the Rayleigh plots, was used to tune the photolytic fractionation (Fig. 4). The εs calculated from two simulations with the original and 1.5 % reduced photolysis rates, which were already optimized for tropospheric values (Sect. 4.2.1 and 4.2.2), were combined to produce the observed εs as follows:

$$\varepsilon_{obs} \approx \varepsilon_{tun} = f_\varepsilon \varepsilon_{org} + (1 - f_\varepsilon)\varepsilon_{red}, \quad (15a)$$

$$J_{tun} = f_\varepsilon J_{org} + (1 - f_\varepsilon)J_{red} = (0.015 f_\varepsilon + 0.985)J_{org}, \quad (15b)$$

where J is the photolysis rate, and the subscripts tun, org, and red indicate tuned, simulated using the original photolysis rate (based on von Hessberg et al., 2004), and 1.5 % reduced photolysis rate ($J_{red} = 0.985 J_{org}$), respectively. We used the 1.5 % reduced photolysis rates only in simulations of $^{14}N^{15}N^{16}O$, $^{15}N^{14}N^{16}O$, and $^{14}N^{14}N^{18}O$, so f_ε for $^{14}N^{14}N^{16}O$ was always 1. The values of f_ε for the heavier isotopocules were calculated by assigning the slope values shown in Fig. 4 to Eq. (15a). The results are shown in Table S1. This approach to tuning the photolytic fractionations is an approximation, as Fig. 4 shows that data scatter in the Rayleigh plots and the slopes (εs) changing with $\ln\{[N_2O]/[N_2O]_0\}$ or altitude, as discussed in Toyoda et al. (2004) and Kaiser et al. (2006). However, we regard this relatively rough tuning approach as sufficient, considering that the main purpose of this study is to reproduce long-term trends of tropospheric N_2O isotopocules and to characterize isotopic signatures of global and hemispheric total sources. We discuss the impact of the photolytic fractionation on the source estimates later.

ACPD
15, 19947–20011, 2015

5 Results and discussion

5.1 Temporal variations at Neumayer station

Figure 5 shows the time series of N_2O mole fraction and $\delta^{15}N^{bulk}$, $\delta^{18}O$, $\delta^{15}N^{\alpha}$, $\delta^{15}N^{\beta}$, and $\delta^{15}N^{sp}$ at NMY, Antarctica, derived from both observations (Röckmann and Levin, 2005) and the optimized model. Standard scales for the observational data are described in Sect. 3.2. The ACTM reproduces the observed results reasonably well overall, showing standard errors of the observational data around the optimize model data (N_2O: 0.1 nmol mol^{-1}, $\delta^{15}N^{bulk}$: 0.005 ‰, $\delta^{18}O$: 0.005 ‰, $\delta^{15}N^{\alpha}$: 0.03 ‰, $\delta^{15}N^{\beta}$: 0.03 ‰, $\delta^{15}N^{sp}$: 0.05 ‰) comparable to or better than those of the measurements (shown by error bars in Fig. 5). The results indicate that the model optimization was successful. In addition, it is also evident that the agreement between the model and the observations is much better for mole fraction, $\delta^{15}N^{bulk}$, and $\delta^{18}O$ than for $\delta^{15}N^{\alpha}$, $\delta^{15}N^{\beta}$, and $\delta^{15}N^{sp}$, as the former components are almost overlapping within the error ranges of the model and observations, whereas the latter components often deviate far from the error ranges. Röckmann and Levin (2005) attributed this data scatter to analytical causes, which make $\delta^{15}N^{\alpha}$ and $\delta^{15}N^{\beta}$ deviate in opposite directions and further enhances $\delta^{15}N^{sp}$ deviation from the model results. This is probably a reasonable explanation, considering that the variability of $\delta^{15}N^{bulk}$ and $\delta^{18}O$ are reasonably simulated by the model despite there being no spatiotemporal variations in the isotopocule ratios of the surface sources given in the model. Meanwhile, Toyoda et al. (2015) showed that $\delta^{15}N^{bulk}$ and $\delta^{18}O$ vary in similar directions depending on various source types, whereas $\delta^{15}N^{sp}$ shows a different tendency from them. Certainly, we cannot exclude the possibility that such features of the site preference data cause more scatter in the atmosphere because of some source-related influence, as Park et al. (2012) raised the possibility that biomass burning was the cause of increased variability in $\delta^{15}N^{\alpha}$ during the El Niño years of 1997–1998. However, in this study we focus on the long-term trends rather than such short-term variations.

ACPD
15, 19947–20011, 2015

Mole fraction and $\delta^{15}N^{sp}$ increase with time, while the other isotopic components decrease. These tendencies are the same as those reported in previous studies, which found that additional input of N_2O from anthropogenic sources with lower $\delta^{15}N^{bulk}$, $\delta^{18}O$, $\delta^{15}N^{\alpha}$, and $\delta^{15}N^{\beta}$, but higher $\delta^{15}N^{sp}$ than those of the tropospheric N_2O, is causing this atmospheric trend; i.e., the so-called Suess effect for N_2O isotopocules (Röckmann et al., 2003; Röckmann and Levin, 2005; Park et al., 2012). Toyoda et al. (2013) showed slightly different trends for $\delta^{18}O$ and $\delta^{15}N^{sp}$ observed at Hateruma station (24° N, 124° E; Table 1; Fig. 1), which is strongly affected by nearby sources in East Asia. Figure 5 also shows long-term change rates for observation and model results. The good agreement is not surprising since the model was optimized to reproduce the observations. In the optimization procedure, only model data for the observation dates were used. For the period 1994–1996, there were five air samples, which were analysed for N_2O and $\delta^{15}N^{bulk}$ (shown by grey color marks in this figure), but not for $\delta^{18}O$, $\delta^{15}N^{\alpha}$ and $\delta^{15}N^{\beta}$ (Röckmann and Levin, 2005). We did not include such observation data in the optimization, because the procedure always needs all four components (N_2O, $\delta^{18}O$, $\delta^{15}N^{\alpha}$, and $\delta^{15}N^{\beta}$) to handle their mole fractions in the calculation (Sect. 2.2). This actually makes only a small difference in the trend, of about 0.01 nmol mol^{-1} a^{-1}, for the N_2O mole fraction, but fortunately, no difference was evident for the isotopic components.

Seasonal cycle patterns are seen especially clearly in the model. So, here we shortly discuss about seasonality for the atmospheric N_2O isotopic components although it is beyond the scope of the paper. The patterns are more irregular in the observations due to measurement errors and possibly due to some natural causes. For the observed $\delta^{15}N^{\alpha}$, $\delta^{15}N^{\beta}$, and $\delta^{15}N^{sp}$, the large scatter means that it is impossible to derive statistically meaningful seasonal cycles. The N_2O mole fraction is highest in autumn to winter, and lowest in spring to summer, the opposite is observed for $\delta^{15}N^{bulk}$ and $\delta^{18}O$, both in the observations and the model. Furthermore, their seasonal amplitudes are also comparable between the observations and model. Our model has seasonally varying oceanic emissions, which has been shown to be important for the

ACPD
15, 19947–20011, 2015

atmospheric N_2O seasonal cycle at middle–high latitudes in the Southern Hemisphere by previous studies. Ishijima et al. (2010) and Thompson et al. (2014b) showed that the emission maximum from the ocean reproduced well the atmospheric N_2O mole fraction maximum in spring at Cape Grim station. The situation is similar at NMY, as there is no significant source south of 40° S except for the ocean. As discussed in Sect. 5.3 and 5.4, the isotopocule ratios of surface sources are always lower than those of atmospheric N_2O; thus, emission maxima simultaneously lead to minima in the isotopocule ratios of the atmospheric N_2O. STE has a similar effect, and it contributes to the mole fraction minimum and isotopocule ratio maximum in autumn by bringing stratospheric air with low-N_2O mole fraction and high isotopocule ratios to the troposphere. We do not examine the mechanisms associated with these seasonal cycles in detail in this study, but our results suggest that our current N_2O isotopocule model may be capable of reasonably simulating seasonal variations in atmospheric N_2O isotopocules.

5.2 Vertical profile in the stratosphere

In this section, we overview how the model simulates stratospheric N_2O isotopocules, but do not go into the details, since the main focus in this study is the tropospheric N_2O. Figure 6 shows vertical profiles of the N_2O mole fraction, $\delta^{15}N^{bulk}$, $\delta^{15}N^{sp}$, and $\delta^{18}O$ in the stratosphere from four selected balloon flights and their model simulations (results of all observations are shown in Fig. S2). The optimized model simulates the observations reasonably well, which decrease in mole fraction and increase in isotopocule ratios with altitude due to photochemical losses (photolysis and reaction with $O(^1D)$) and the associated isotopocule fractionation. The model simulations with the original and 1.5 % reduced photolysis rates (Sect. 4.2.3) tend to under- and over-estimate the vertical gradient of $\delta^{15}N^{bulk}$ and $\delta^{18}O$, respectively. The figure also shows how the photolytic fractionation tuning modifies the apparent fractionation constant ε (Fig. 4). Although no offset was applied to the model and observation data shown in Figs. 5 and 6 (and S2), the model does not show significant biases compared with the observations throughout the atmosphere from the surface to the stratosphere.

ACPD
15, 19947–20011, 2015

The model significantly underestimates the vertical gradients of N_2O mole fraction by about 20 % and isotopocule ratios by about 60 % over Kiruna. During the balloon observations, almost all air samplings were conducted within the polar vortex. The vortex prevents the air outside the vortex, with a higher N_2O mole fraction and lower isotopocule ratios, from being transported into the vortex, thus creating a large gradient across the vortex region sometimes exceeding 100 nmol mol^{-1} in mole fraction around 25 km altitude (Greenblatt et al., 2002). Also, the thermal exchange is disturbed, so the upper altitude air, which has a lower N_2O mole fraction and higher isotopocule ratios, is downwelling due to the strong radiative cooling, thereby contributing to the gradient across the vortex. The ACTM tends to simulate a weaker polar vortex than is actually the case. This feature has already been discussed by Ishijima et al. (2010), who compared ACTM results with the Aura Microwave Limb Sounder (Aura-MLS) satellite N_2O mole fraction data, and showed that the ACTM overestimated the stratospheric mole fraction in the polar vortex in the winter hemisphere. Therefore, this model transport deficiency probably causes the overestimation of the N_2O mole fraction and underestimation of the isotopocule ratios over Kiruna. In the polar vortex, chemical losses of N_2O are very weak due to less sunlight, so variations of N_2O isotopocules in the vortex are mostly determined by transport of the air-mass outside the vortex. It means that εs in the vortex strongly reflect those outside the vortex. In fact, εs over Kiruna (Fig. S3) show good agreement between the observations and the model, indicating that the chemistry is reasonable but that the transport makes the profiles unrealistic.

We also need to consider the possibility that the overestimation of mole fraction and underestimation of isotopocule ratios in the polar vortex affect the tropospheric N_2O through STE. However, we do not regard this aspect of the ACTM as too serious with respect to reproducing long-term trends of N_2O isotopocules in the troposphere and estimating the isotopic signatures of the surface sources. Our optimized model shows the troposphere–stratosphere N_2O flux of 66 Tg a^{-1} N and the stratosphere–troposphere N_2O flux of 54 Tg a^{-1} N (calculated using values in Table S3), which are quite similar to those calculated in Toyoda et al. (2013). Considering that the ratio of

ACPD
15, 19947–20011, 2015

N_2O mass in the polar region to that in mid-high latitudes, where the stratosphere–troposphere fluxes occur, is about 10 %, the fluxes for the period of the strong polar vortex is 3 Tg a^{-1} N, assuming the fluxes contribute to the annual fluxes by 50 %. Considering pressure weighted mean differences of the mole fraction and $\delta^{15}N^{bulk}$ in the altitude range of 10–15 km, which in important for the STE, are about 20 nmol mol^{-1} and −1 ‰ ([model] – [observation]), respectively (Fig. 6), the model is supposed to underestimates the iso-flux from the stratosphere to the troposphere in the polar region by about 2 Tg a^{-1} N ‰. It can be translated into about 0.1 ‰ overestimation of $\delta^{15}N^{bulk}$ in the final isotopic estimate of the global total sources in this study (Table 4). Here, the relative contribution of the polar region to the stratosphere–troposphere fluxes is uncertain, but trebling the contributing ratio leads to 0.4 ‰ overestimation of $\delta^{15}N^{bulk}$ in the isotopic estimate of the global total sources. It is obviously the maximum case, so it is thought that the uncertainty in the final source estimation due to the model deficiency for simulating the vertical profiles in the polar vortex is smaller than that due to the measurement. There is also the possibility that seasonal variations of the N_2O isotopic compositions in the troposphere are weakened in the model due to the underestimation of the vertical profiles in the polar stratosphere. However, we need more specific modelling and analysis to discuss the issue, which is also beyond the scope of this study.

In terms of the global budget of N_2O, the vertical profiles in the tropical and mid-latitude stratosphere are more important. N_2O enters the stratosphere in the tropics by convective uplift, and is then transported to higher altitudes/latitudes mainly by the Brewer–Dobson circulation. In this way, N_2O is decomposed by photochemical reactions, and suffers from kinetic isotopic fractionation. As a result, the N_2O mole fraction decreases and isotopocule ratios increase at higher altitudes/latitudes (Fig. S4). This latitudinal and vertical structures of the N_2O mole fraction and isotopocule ratios are reasonably reproduced by the model, except over Kiruna (Figs. 6 and S2). Over Hyderabad, India, the vertical gradients are small, because N_2O is not as exposed to photochemical losses just after entering the stratosphere across the tropopause at around

ACPD
15, 19947–20011, 2015

17 km. The fact that the vertical gradients around the entrance to the stratosphere are well reproduced indicates that the dynamical STE rate and chemical loss rates for N_2O are realistic in the ACTM. In particular, convective upward transport in the tropics has a large impact on the global N_2O budget, because the amount of chemically broken N_2O is highly dependent on that of N_2O brought into the stratosphere. Good reproducibility at mid to high latitudes over Sanriku, Japan, and Syowa, Antarctica, where the vertical gradients are greatly enhanced because of the longer timespan available for N_2O to be affected by loss reactions, means that the balance between poleward and upward transports, represented by the Brewer–Dobson circulation, and chemical loss is reasonable in the model. We conclude that based on the results shown in Sect. 5.1 and 5.2, the ACTM is capable of realistically simulating circulation and chemistry of the N_2O isotopocules through the atmosphere, at least from near the surface to the stratosphere.

5.3 Latitudinal gradient in the troposphere

Figure 7 shows the mean latitudinal distributions of the atmospheric N_2O mole fraction and isotopocule ratios from the observations and optimized model for the period 1991–2001, together with the total N_2O emissions and source isotopocule ratios estimated by the optimization. As a validation for the N_2O mole fraction, the mean distribution derived from monthly observation data from five stations by the Global Atmospheric Gases Experiment (GAGE)/the Advanced Global Atmospheric Gases Experiment (AGAGE) (Table 1; Fig. 1) are also shown. We selected this dataset because the AGAGE standard scale was used for the measurements at NMY. Details of the data processing are described in the Supplement. It can be seen that the model nicely reproduces the latitudinal distribution of the observed mole fractions almost within the uncertainty (95 % confidence range). In the mole fraction transition zone from 30° S to 0°, the Intertropical Convergence Zone (ITCZ) and South Pacific Convergence Zone (SPCZ) present mixing barriers between the Northern Hemispheric high N_2O air and Southern Hemispheric low N_2O air, which leads to a clear latitudinal gradient (e.g., Ishi-

ACPD
15, 19947–20011, 2015

jima et al., 2009). The latitudinal gradient is also very close to those reported in Huang et al. (2008) of about 1.5 nmol mol^{-1} with the maximum in northern mid-latitudes. At NMY (71° S) and the firn air measurement sites (75° N and 73° S), the values from the observations and optimized model are not completely the same, despite the model being optimized by the data (Sect. 4.2). This is because only the model data that coincided with the observation dates were fitted to the observation data by the optimization, while, in Fig. 7, the means of the observation data smoothed by a digital low-pass filter and of the daily mean model outputs (both for 1991–2001) are plotted.

For the isotopocule ratios, there is no independent data available to validate the optimized model results. In Fig. 7, the firn measurement data are adjusted to the means of the optimized model results at Dome Fuji and H72 (73° S) to correct for the isotopic standard scale difference between the NMY data and the firn data, but agreement between the model and observations is not perfect for the same reason explained above for mole fraction. The most outstanding features of the atmospheric N_2O isotopocule ratios are probably the large uncertainty ranges in the Northern Hemisphere. This can be attributed to optimization and the error estimation method. As mentioned above, the model is first optimized to reproduce the NMY data, and then optimized for the north–south gradient using the firn data. Therefore, the uncertainty in the Southern Hemisphere is small because of the high-precision measurements from the NMY, but the error range in the Northern Hemisphere is determined by the sum of the errors from NMY, NGR, and DFJ/H72 (Table 3). This is inevitable as long as there is only a single dataset available to determine the present north–south gradient of the atmospheric N_2O isotopocule ratios (Ishijima et al., 2007) and assuming that the highest-precision measurement at the NMY is true. For example, in the uncertainty estimation of $\delta^{18}O$, if the uppermost value from Antarctica (+0.07 ‰, Fig. 7c and Table 3) and the lowermost value (−0.05 ‰) from the Arctic are taken, the 95 % confidence range becomes 0.17 ‰ ($= 1.96 \times \sqrt{(0.07^2 + 0.05^2)}$), although the root square part was actually the standard deviation of the 100 000 Gaussian distribution errors. Here, the errors for the firn data

ACPD
15, 19947–20011, 2015

are the standard errors of the measurement data around the long-term trend derived by a spine fitting curve to the data (Ishijima et al., 2007; the Supplement).

Table 3 indicates that the interhemispheric gradients of atmospheric N_2O mole fraction and isotopocule ratios in the optimized model are slightly smaller than the observed interpolar gradients. We attribute this to the latitudinal gradients as well as the vertical gradients within the hemisphere (Fig. 8), because the firn air samples were collected from stations at high elevations in high latitudes, such as NGR at 75° N/2959 m a.s.l., and DFJ at 77° S/3810 m a.s.l. (Table 1), and there are some gradients from the equator to the poles, especially significantly in the Southern Hemisphere (Fig. 7). Figure 8 shows that the ACTM realistically simulates these latitudinal and vertical distributions, which are produced by isotopically lighter N_2O emitted from surface sources and isotopically heavier N_2O mixed-in from the stratosphere. The vertical gradients in the troposphere are actually very small, showing the maximum gradients, between the surface and 8 km altitude, of about 1.3 nmol mol^{-1}, 0.07 and 0.06 ‰ for mole fraction, $\delta^{15}N^{bulk}$, and $\delta^{18}O$, respectively, in the polar regions, and even small being almost zero in the tropics, where convective transport is quickly bringing near surface N_2O to the upper troposphere and further into the stratosphere. Magnitudes of the vertical gradients are comparable to those of the interhemispheric gradients (Table 3), and important for hemispheric source estimates using the atmospheric observational data from high elevation firn stations in the polar regions. As the model data at the locations of the firn stations were used for our model optimization, we expect that the 3-D model-based estimates of the isotopic signature of the sources could differ from the estimates made using a two-box model, in which the interhemispheric differences are directly derived from the firn measurement data (Toyoda et al., 2013). This would be important if we wished to translate the atmospheric observation data into the surface source information as precisely as possible, as is the case in inverse modelling (Hirsch et al., 2006; Huang et al., 2008; Thompson et al., 2014c).

Optimization of the atmospheric values was achieved by adjusting the global and hemispheric total emissions of four N_2O isotopocules. As explained in Sect. 4.1.3,

ACPD
15, 19947–20011, 2015

the optimization modifies the hemispheric total emissions but does not modify the emission distributions within the hemisphere; as a result, the isotopocule ratios from the sources become homogeneous in each hemisphere (Fig. 7). $\delta^{15}N^{bulk}$ of the total sources shows reasonable results of 10 ‰ lower in the Northern Hemisphere than in the Southern Hemisphere because there are more land sources with relatively lower $\delta^{15}N^{bulk}$ (Toyoda et al., 2015) in the Northern Hemisphere, while the area of the ocean with relatively higher $\delta^{15}N^{bulk}$ is larger in the Southern Hemisphere. Interestingly, despite almost the same $\delta^{18}O$ levels in both hemispheric total sources, the $\delta^{18}O$ of the atmospheric N_2O is lower in the Northern Hemisphere. This can be simply explained by the dilution of isotopically heavier tropospheric N_2O by lighter N_2O emitted from surface sources when Northern Hemispheric emissions are larger, given even isotopocule fractionation caused by the stratospheric chemical loss in both hemispheres. In fact, the interhemispheric transport smoothes out the north–south gradient to some extent, but the tendency would not change. The $\delta^{15}N^{sp}$ shows completely the opposite tendency, the same atmospheric $\delta^{15}N^{sp}$ values in both hemispheres (assumed only for the optimization, see Sect. 4.2.2), but the source $\delta^{15}N^{sp}$ is higher in the Northern Hemisphere. The logic is exactly the same as that for $\delta^{18}O$, but in this case the extra $\delta^{15}N^{sp}$ input from the surface sources increases the atmospheric value in the Northern Hemisphere. We note that the north–south gradients in the atmosphere, as well as the emissions and isotopic signatures of surface sources, are highly dependent on the transport features of the model, such as interhemispheric transport, convection, and STE, as well as the emission distribution used in the model. On these points, the ACTM shows the best result of north–south gradient for the atmospheric N_2O mole fraction in comparison with other models (Thompson et al., 2014b, c); therefore, the N_2O isotopocule ratios are also expected to be reliable, both in the atmosphere and for top-down source estimates.

ACPD
15, 19947–20011, 2015

5.4 Estimation of emissions and isotopocule ratios for total sources in each hemisphere

Table 4 summarizes the top-down and bottom-up estimates of emissions and isotopocule ratios for the global, northern, and southern hemispheric total sources in this and previous studies (all properties in the optimized model are shown in Table S3). Top-down estimates of the global total emissions are relatively consistent, although the result of Park et al. (2012; 17.7 $\mathrm{Tg\,a^{-1}}$ N) is slightly larger and closest to the recent bottom-up basis estimate of Ciais et al. (2013). These results are highly dependent on what kind of model is used (e.g., one-box, two-box or global 3-D model) as well as parameters used in the model, such as N_2O lifetime, STE-rate, since atmospheric burden and growth rate, which are based on the atmospheric observation data, are very similar in all studies. Our estimate is based only on the ACTM simulations, but such chemistry transport models still show some differences in the global total emissions because of the differences in the atmospheric transport and chemical loss rate etc. Thompson et al. (2014c) show that inverse estimates of global annual emissions for the period 2006–2008 by five different models range from 15 to 19 $\mathrm{Tg\,a^{-1}}$ N. Compared with these, the box model estimates fall within a relatively narrow range, and this is probably because their simple structures straightforwardly reflect the atmospheric observation results.

Top-down estimates of $\delta^{15}N^{bulk}$ of the global total sources are mostly within ±1 ‰, although Toyoda et al. (2013) reported a slightly lower value, because of the different growth rate observed, probably due to strong continental sources combined with seasonal monsoonal transport of the source signals at Hateruma station (Table 1; Fig. 1), as well as a different observational period. Inter-institute differences in the standard scale used for isotopic measurements are probably not larger than 0.5 ‰, and are thus not a significant factor in these comparisons, because the isotopic signature of the total sources is mostly determined by the growth rates of atmospheric N_2O mole fraction and the isotopocule ratios in top-down estimates. The values of $\delta^{18}O$ and $\delta^{15}N^{sp}$ are

ACPD
15, 19947–20011, 2015

vary slightly more between studies, mainly because of the relatively large measurement errors. We also calculated a bottom-up estimate, based on the source isotopic signatures compiled by Toyoda et al. (2015; see Table S4). In principle, the mean isotopic value of a certain area of N_2O sources is supposed to be the sum of the isotopic ratios weighted by the emissions, which are actually observed at the sources. However, at present, isotopic measurements of N_2O sources are relatively limited in terms of spatiotemporal representativeness and coverage of source categories and show large differences even within single source categories. Therefore, as a first-order approximation, we calculated simple averages for the isotopocule ratios of the individual sources (Table S4), which were compiled by Toyoda et al. (2015; Fig. 9), and then summed them weighted by the corresponding source strength used in our simulations (Sect. 4.1.3). Thus calculated, the global mean $\delta^{15}N^{bulk}$ and $\delta^{15}N^{sp}$ agree closely with our top-down estimates within 0.3 ‰, whereas $\delta^{18}O$ is higher than our value, mainly because of the high averaged $\delta^{18}O$ value of the ocean emissions (49 ‰ and 3.6 Tg a^{-1} N). This rough estimate contains large uncertainties of 9 to 15 ‰, but the satisfactory agreement indicates that the ranges of the measured isotopic values of the sources and emissions based on the inventories are realistic.

Our estimates of hemispheric sources show an interhemispheric difference of about 10 ‰ for $\delta^{15}N^{bulk}$, whereas $\delta^{18}O$ was estimated to be the same in both hemispheres. The associated uncertainties, which are 11.4 and 22.6 ‰ for the interhemispheric differences of $\delta^{15}N^{bulk}$ and $\delta^{18}O$, respectively, based on the law of propagation of errors, are rather large, but smaller for $\delta^{15}N^{bulk}$ compared to $\delta^{18}O$ because of better measurement precision (Table 3). To date, only one study has attempted a top-down estimate of the isotopocule ratios of both hemispheric total sources (i.e., Toyoda et al., 2013), and its results differ somewhat from the results of this study. The difference in the absolute $\delta^{18}O$ values is due to the fact that the atmospheric trend was based on a different dataset. Toyoda et al. (2013) estimated an interhemispheric difference of the total sources of about 1 ‰, which is in good agreement with the negligible difference from our model study, considering the huge range of $\delta^{18}O$ from the various sources

ACPD
15, 19947–20011, 2015

(Toyoda et al., 2015). The interhemispheric difference in $\delta^{15}N^{bulk}$ estimated by Toyoda et al. (2013; about 4 ‰) is slightly smaller than ours (about 10 ‰). This can be attributed to differences in several factors, such as latitudinal and vertical transports (interhemispheric and stratosphere–troposphere exchanges) and distributions (interhemispheric and vertical gradient), which are explicitly simulated in the ACTM but assumed in the two-box model of Toyoda et al. (2013). The latitudinal emission distribution in our model (Fig. 7) also has a significant influence on these hemispheric-scale estimates based on the atmospheric observation data, as discussed in Sect. 5.3. Tendencies for our bottom-up estimates, in which both $\delta^{15}N^{bulk}$ and $\delta^{18}O$ of the total sources are higher in the Southern Hemisphere than in the Northern Hemisphere, are similar to those of Toyoda et al. (2013). As expected, the results directly reflect the fractions of isotopically lighter natural and anthropogenic soil emissions, and of isotopically heavier oceanic emissions, in each hemisphere; more land and less ocean in the Northern Hemisphere, and less land and more ocean in the Southern Hemisphere make the total sources isotopically lighter and heavier, respectively.

We also examined the sensitivities of the emissions and isotopocule ratios of the hemispheric total sources to interhemispheric differences in the atmospheric N_2O mole fraction and isotopocule ratios in our top-down estimates. In these experiments, we assumed interhemispheric differences in the atmospheric N_2O mole fraction and/or isotopocule ratios to be more or less than the real by 50 % by changing the values observed (Table 3), and then optimized the Northern Hemisphere to Southern Hemisphere emission ratio in the model (Sect. 4.2.2; Fig. 2) to reproduce the assumed interhemispheric differences in the atmosphere. Figure 9 (top) indicates that even when emissions in both hemispheres are the same, the mole fraction is higher by about 0.6 nmol mol^{-1} in the Northern Hemisphere. This is mainly caused by the latitudinal emission distribution used in the model, in which more emissions are located at higher latitudes in the Northern Hemisphere (Fig. S1c). For example, as an extreme case, if the same amount of N_2O is emitted only at the North Pole and in the tropics of the Southern Hemisphere over a period of time, the N_2O mole fraction would always be

ACPD
15, 19947–20011, 2015

higher in the Northern Hemisphere, because it takes several months for N_2O in the Arctic to reach to the equator while N_2O emitted in the tropics quickly diffuses into both hemispheres and partly into the stratosphere. These latitudinal and vertical transportations of the emitted N_2O are also highly model-dependent (Denning et al., 1999). Similar to the above case, the atmospheric N_2O isotopocule ratios are lower in the Northern Hemisphere than in the Southern Hemisphere, even when there is no interhemispheric difference in the N_2O emissions (corresponding to zero on the y axis in Fig. 9, top, and to the sensitivity line between the thick solid and dashed lines in Fig. 9, bottom) and in the isotopocule ratios of the total sources (corresponding to zero on the y axis in Fig. 9, bottom). The features are also thought to originate from latitudinal emission distribution in our model (Fig. 7). As expected, the sensitivity of the atmospheric gradient to changes in the hemispheric source values is almost the same for $\delta^{15}N^{bulk}$ and $\delta^{18}O$, but also for $\delta^{15}N^{sp}$, with the slopes of all lines being similar (240 ± 10 ‰‰$^{-1}$ in Fig. 9, bottom). These results indicate that the interhemispheric gradient of the N_2O isotopocule ratio is determined almost completely by the emissions in both hemispheres and interhemispheric transport, and much less so by the influence of stratospheric chemistry, which could alter $\delta^{15}N^{bulk}$, $\delta^{18}O$, and $\delta^{15}N^{sp}$ in each direction by each kinetic fractionation after emitted from surface sources into the atmosphere.

5.5 Time series of atmospheric N_2O isotopocule ratios at other stations

Figure 10 shows the atmospheric N_2O mole fraction and isotopocule ratios obtained from ground-based observations, firn air analysis, and the optimized model. The trends in the observed mole fraction are reasonably simulated for all stations, but some biases between observations and between observations and model are evident. In the 20th century, the firn data from DFJ and H72 tend to be lower than the observations and model results at NMY. This is likely due to the difference in the standard scales used for the measurements at each station, as the long-term trend is optimized only to the NMY data for the period 1990–2002. After 2000, the model seems to under-

ACPD
15, 19947–20011, 2015

estimate the mole fraction observed at HAT, NAL, and CGO. This is probably related to the emission trend in the model (seen in Fig. S1), represented by anthropogenic emissions from the EDGARv4.2 and EDGARv4.2 FT2010, and by biomass burning emissions from GFED3.1. It seems that the increase in emissions over the period 1997–1998 (Fig. S1a) causes small increase of the model mole fraction around 1999 and stagnation of the increasing trend after that period, especially in the Southern Hemisphere (Fig. 10). Furthermore, in the optimization procedure, the model results, including the period of elevated mole fraction, are fitted to the observation data at NMY; as a result, the model mole fractions are slightly underestimated when compared with the observations after 2000. The episodic increase in emissions is derived from two different inventories used in our simulations; namely, indirect emissions of NO_x and NH_3 from EDGAR4.2, and biomass burning from GFED3.1. NH_3 emissions in 1997 in EDGAR4.2 are two to three times higher than in other years owing to almost exclusively due to peat and forest fires in Indonesia. It is well known that drought led to strong biomass burning during the strong El Niño in 1997–1998 in the region, but it is difficult to judge how realistic the emission estimates by EDGAR4.2 and GFED3.1 are here. According to Nevison et al. (2007), the growth rate of N_2O mole fraction at CGO decreases for the El Niño period. These results may be reasonable because El Niño and the subsequent drought cause a decrease in oceanic upwelling emissions and soil emissions, respectively. Park et al. (2012) also discussed about the biomass burning emissions as a possible cause of the $\delta^{15}N^{\alpha}$ anomaly for the period. From this perspective, the observations at NMY show high mole fraction and $\delta^{18}O$ and low $\delta^{15}N^{bulk}$ and $\delta^{15}N^{sp}$ on 07 December 1997 (Fig. 5). For N_2O emitted from biomass burning, Toyoda et al. (2015) found high $\delta^{15}N^{bulk}$ and $\delta^{15}N^{sp}$ but low $\delta^{18}O$, while our backward trajectory analysis did not present clear evidence that the air mass came to NMY from low latitudes on that date. More specific analysis will be needed to examine such source signals in the atmospheric N_2O isotopocule ratios.

It is obvious that the observation results for $\delta^{15}N^{bulk}$, $\delta^{18}O$, and $\delta^{15}N^{sp}$ reported by Röckmann and Levin (2005) are exceptionally stable compared with other observa-

ACPD
15, 19947–20011, 2015

tions, which show greater temporal variability. The model optimized to the NMY data seems to simulate the long-term trends of $\delta^{15}N^{bulk}$, $\delta^{18}O$, and $\delta^{15}N^{sp}$ reasonably well for all stations, but the systematic differences between the observations, and between the observations and the model results, are remarkable. These systematic differences are mainly related to inter-institute differences in the standard scales used, considering that the interhemispheric gradients of $\delta^{15}N^{bulk}$ and $\delta^{18}O$ in the troposphere is of the order of 0.1 ‰ or less, as also seen in the model results in Fig. 10. Mohn et al. (2014) showed results for common N_2O samples distributed to each institute and analysed for $\delta^{15}N^{bulk}$, $\delta^{18}O$, and $\delta^{15}N^{sp}$, which were widely spread when based on the original standard scale used by each institute. As shown above, our model seems to be able to simulate atmospheric N_2O isotopocule ratios with an accuracy of approximately 0.01 ‰. This means that, if we try to use the atmospheric N_2O isotopic data to better constrain N_2O sources, the observation data are also required to be of a comparable precision and accuracy. A common scale for all observations is required to use the data, which is obtained at great effort, for more quantitative studies. We suggest that a very careful scale intercalibration is required as follows.

1. Common gases, which are circulated to individual institutes for the intercalibration, should contain natural or slightly artificially modified ambient air to establish and quantify non-negligible effects of minor components originally contained in atmospheric samples in the N_2O isotopocule analysis.

2. Multiple gases with different N_2O mole fractions and isotopocule ratios (ideally covering the full range of the atmospheric values) should be prepared to calibrate for non-linear relation between electric output signals by the measurement system and actual mole fraction or isotopocule ratios of the sample.

3. The common gases should be analysed in completely the same manner as usual atmospheric samples.

Sensitivity tests by our model (Sect. 5.4) suggested that an accuracy of measurements for atmospheric N_2O isotopocule delta values better than 0.03 ‰ is required (following

ACPD
15, 19947–20011, 2015

the law of propagation of error) to estimate the isotopocule ratios of hemispheric total sources with an accuracy of 10 ‰. In addition, for example, in order to estimate monthly emissions of the N_2O isotopic compositions at regional scale, improvements especially for measurement frequency and number of the stations as well as the inter-calibration of the standard would be necessary, assuming that the analytical precisions are those for the NMY data. If successful, it would allow us to incorporate more observation data into our model, thereby enabling improved optimization and more advanced inverse estimation of surface source emissions in the near future.

6 Conclusions

We developed an atmospheric N_2O isotopocule model by incorporating isotopocule fractionation caused by photolysis and oxidation by $O(^1D)$, together with surface fluxes of N_2O isotopocules, in a chemistry-coupled atmospheric general circulation model (ACTM). In addition, we developed a method, based on multi-scenario simulations, to optimize the model for long-term trends, north-to-south gradients in the troposphere, and apparent fractionation constants in the stratosphere, by using atmospheric data obtained from ground-based stations, firn air analysis, and balloon and aircraft observations in the stratosphere. This is the first study to simulate atmospheric N_2O isotopocules using a 3-D chemistry transport model with explicitly prescribed surface fluxes, and to optimize the model using atmospheric observation data.

The optimized model reasonably reproduced the atmospheric N_2O mole fraction and isotopocule ratios observed at Neumayer station, Antarctica, especially the long-term trends; this indicates that the model optimization was successful. Temporal variability in mole fraction, $\delta^{15}N^{bulk}$, and $\delta^{18}O$, including seasonal and synoptic variations, were also comparable between the observations and the optimized model, whereas the simulated $\delta^{15}N^{\alpha}$, $\delta^{15}N^{\beta}$, and $\delta^{15}N^{sp}$ were much more stable than the highly scattered observations. The model showed regular seasonal cycles for all components, which are produced by seasonality in oceanic emissions and by atmospheric transport, re-

ACPD
15, 19947–20011, 2015

producing observations in mole fraction and $\delta^{15}N^{bulk}$ relatively well, but the cycles were not as clear in the other observed isotopic components.

The model reproduced the vertical profiles of N_2O mole fraction and isotopocule ratios in the stratosphere reasonably well, which decrease and increase with increasing altitude, respectively. Tuning of photolytic fractionation, using apparent fractionation constants (εs), improved the model results by slightly increasing the vertical gradients of the isotopocule ratios. However, in the polar vortex, the model significantly underestimated the vertical gradients of both mole fraction and isotopocule ratios by about 20 and 60 %, respectively. This was caused by excess transport of air with high N_2O mole fraction and low isotopocule ratios from lower latitudes into the vortex, as the model has insufficient dynamic isolation.

Optimization of the north–south gradient was successfully done. The mean latitudinal gradient of atmospheric N_2O mole fraction for the period 1991–2001 in the optimized model was consistent with that of independent observational data from GAGE/AGAGE within the uncertainty range. Although there are no independent data available with which to validate latitudinal gradients of optimized isotopocule ratios, we found that the model could reasonably simulate the vertical and latitudinal gradients within the hemispheres. The fact that the respective interhemispheric differences of 1 nmol mol^{-1}, 0.1 and 0.04 ‰ for mole fraction, $\delta^{15}N^{bulk}$ and $\delta^{18}O$ were smaller than the respective interpolar differences of 1.3 nmol mol^{-1}, 0.12 and 0.06 ‰ was due to the vertical and latitudinal distributions within the hemispheres. The tropospheric vertical gradients between the surface and 8 km altitude were 1.3 nmol mol^{-1}, 0.07 and 0.06 ‰ for mole fraction, $\delta^{15}N^{bulk}$, and $\delta^{18}O$, respectively, in the polar regions, and are comparable to the interhemispheric gradients. The gradients are very small, but are important for isotopically characterizing surface sources using atmospheric observation data from the locations of the individual stations. Such tropospheric latitudinal and vertical gradients lead to differences in the isotopic characterization of hemispheric total sources when compared with a simple two-box model, which in some cases directly uses station data as the hemispheric representative values. The 3-D structures simulated by the model

ACPD
15, 19947–20011, 2015

are important to incorporate atmospheric observation data as realistically as possible and to quantify surface sources precisely.

This study reports the first 3-D model-based top-down estimates of hemispheric source signatures. The resultant interhemispheric differences in the isotopocule ratios for hemispheric total sources ([Northern Hemisphere] – [Southern Hemisphere]) were about −10 ‰ for $\delta^{15}N^{bulk}$, but almost zero for $\delta^{18}O$. The near-zero $\delta^{18}O$ result is similar to that obtained from a previous two-box model (Toyoda et al., 2015), but the interhemispheric difference in $\delta^{15}N^{bulk}$ calculated in this study is more than twice that of the previous estimate. This was caused by the differences in the above-mentioned latitudinal and vertical distributions of tropospheric N_2O isotopocule ratios, in transport such as interhemispheric and stratosphere–troposphere exchange rates, and in the latitudinal distribution of surface emissions in the model. The sensitivity of the atmospheric gradient to hemispheric-scale source estimates by the model optimization was very similar among $\delta^{15}N^{bulk}$, $\delta^{18}O$, and $\delta^{15}N^{sp}$. Our results indicate that surface emissions and tropospheric transport are the main controls on atmospheric gradients, whereas isotopocule fractionation by stratospheric chemistry and stratosphere-to-troposphere N_2O transport are less important.

The ability of the model to simulate detailed temporal and spatial variability in atmospheric N_2O isotopocule ratios suggests the need for more careful inter-calibration of the standard scales, as well as constructing a global network of the high-precision, high-frequency measurements. These improvements could contribute to providing a more complete and precise picture of spatiotemporal variations in atmospheric N_2O isotopocules and could expand the ongoing development of N_2O inverse modelling to include also isotopic information.

The Supplement related to this article is available online at doi:10.5194/acpd-15-19947-2015-supplement.

ACPD
15, 19947–20011, 2015

Acknowledgements. We thank Ronald G. Prinn (MIT), Ray Weiss (UCSD-SIO), Paul Krummel (CSIRO) and Simon O'Doherty (Bristol University) and their AGAGE team colleagues for providing AGAGE data. The AGAGE stations used here are supported principally by NASA (USA) grants to MIT and SIO, and also by DECC (UK) and NOAA (USA) grants to Bristol University, and by CSIRO and BoM (Australia). We are grateful to Sunyoung Park, Phillip Croteau, and Kristie A. Boering for making their N_2O isotopocule observation data from Cape Grim station available in their paper. We thank A. F. Lex Bouwman, Cynthia Nevison and Xin Jin for providing their oceanic flux data. We extend our thanks to anonymous reviewers for their helpful comments. This work was partly supported by JSPS KAKENHI grant numbers 22241008, 23710034, and 25241006, and also by Global Environmental Research Fund (A-0904) of the Ministry of the Environment, Japan.

References

Akiyoshi, H., Zhou, L. B., Yamashita, Y., Sakamoto, K., Yoshiki, M., Nagashima, T., Takahashi, M., Kurokawa, J., Takigawa, M., and Imamura, T.: A CCM simulation of the breakup of the Antarctic polar vortex in the years 1980–2004 under the CCMVal scenarios, J. Geophys. Res., 114, D03103, doi:10.1029/2007JD009261, 2009.

Bernard, S., Röckmann, T., Kaiser, J., Barnola, J.-M., Fischer, H., Blunier, T., and Chappellaz, J.: Constraints on N_2O budget changes since pre-industrial time from new firn air and ice core isotope measurements, Atmos. Chem. Phys., 6, 493–503, doi:10.5194/acp-6-493-2006, 2006.

Bouwman, A. F., Van der Hoek, K. W., and Olivier, J. G. J.: Uncertainties in the global source distribution of nitrous oxide, J. Geophys. Res., 100, 2785–2800, 1995.

Brenninkmeijer, C. A. M. and Röckmann, T.: Mass spectrometry of the intramolecular nitrogen isotope distribution of environmental nitrous oxide using fragment-ion analysis, Rapid Commun. Mass Sp., 13, 2028–2033, 1999.

Ciais, P., Sabine, C., Bala, G., Bopp, L., Brovkin, V., Canadell, J., Chhabra, A., DeFries, R., Galloway, J., Heimann, M., Jones, C., Quéré, C. L., Myneni, R. B., Piao, S., and Thornton, P.: Carbon and other biogeochemical cycles, in: Climate Change 2013: The Physical Science Basis. Contribution of Working Group I to the Fifth Assessment Report of the Intergovern-

ACPD
15, 19947–20011, 2015

mental Panel on Climate Change, Cambridge University Press, Cambridge, UK and New York, NY, USA, 2013.
Coplen, T. B.: Guidelines and recommended terms for expression of stable-isotope-ratio and gas-ratio measurement results, Rapid. Commun. Mass Sp., 25, 2538–2560, 2011.
Denning, A. S., Holzer, M., Gurney, K. R., Heimann, M., Law, R. M., Rayner, P. J., Fung, I. Y., Fan, S.-M., Taguchi, S., Friedlingstein, P., Balkanski, Y., Taylor, J., Maiss, M., and Levin, I.: Three-dimensional transport and concentration of SF6. Tellus B, 51, 266–297, doi:10.1034/j.1600-0889.1999.00012.x, 1999.
Dlugokencky, E. J., Steele, L. P., Lang, P. M., and Masarie, K. A.: The growth rate and distribution of atmospheric methane, J. Geophys. Res., 99, 17021–17043, doi:10.1029/94JD01245, doi:10.1029/94JD01245, 1994.
Dragani, R.: On the quality of the ERA-Interim ozone reanalyses: comparisons with satellite data, Q. J. Roy. Meteor. Soc., 137, 1312–1326, 2011.
Greenblatt, J. B., Jost, H., Loewenstein, M., Podolske, J., Bui, T. P., Hurst, D., Elkins, J. W., Herman, R. L., Webster, C. R., Schauffler, S., Atlas, E., Newman, P., Lait, L. R., Müller, M., Engel, A., and Schmidt, U.: Defining the polar vortex edge from an N_2O potential temperature correlation, J. Geophys. Res., 107, 8268, doi:10.1029/2001JD000575, 2002.
Griffith, D. W. T., Parkes, S. D., Haverd, V., Paton-Walsh, C., and Wilson, S. R.: Absolute calibration of the intramolecular site preference of ^{15}N fractionation in tropospheric N_2O by FT-IR spectroscopy, Anal. Chem., 81, 2227–2234, doi:10.1021/ac802371c, 2009.
Hirsch, A. I., Michalak, A. M., Bruhwiler, L. M., Peters, W., Dlugokencky, E. J., and Tans, P. P.: Inverse modeling estimates of the global nitrous oxide surface flux from 1998–2001, Global Biogeochem. Cy., 20, GB1008, doi:10.1029/2004GB002443, 2006.
Huang, J., Golombek, A., Prinn, R. G., Weiss, R., Fraser, P., Simmonds, P., Dlugokencky, E. J., Hall, B., Elkins, J., Steele, P. L., Langenfelds, R., Krummel, P., Dutton, G., and Porter, L.: Estimation of regional emissions of nitrous oxide from 1997 to 2005 using multinetwork measurements, a chemical transport model, and an inverse method, J. Geophys. Res., 113, D17313, doi:10.1029/2007JD009381, 2008.
Ishijima, K., Sugawara, S., Kawamura, K. Hashida, G., Morimoto, S., Murayama, S., Aoki, S., and Nakazawa, T.: Temporal variations of the atmospheric nitrous oxide concentration and its $\delta^{15}N$ and $\delta^{18}O$ for the latter half of the 20th century reconstructed from firn air analyses, J. Geophys. Res., 112, D03305, doi:10.1029/2006JD007208, 2007.

ACPD
15, 19947–20011, 2015

Ishijima, K., Nakazawa, T., Sugawara, S., and Aoki, S.: Variations of atmospheric nitrous oxide concentration in the northern and western Pacific, Tellus B, 61, 408–415, 2009.
Ishijima, K., Patra, P. K., Takigawa, M., Machida, T., Matsueda, H., Sawa, Y., Steele, P. L., Krummel, P. B., Langenfelds, R. L., Aoki, S., and Nakazawa, T.: Stratospheric influence on the seasonal cycle of nitrous oxide in the troposphere as deduced from aircraft observations and model simulations, J. Geophys. Res., 115, D20308, doi:10.1029/2009JD013322, 2010.
Jin, X. and Gruber, N.: Offsetting the radiative benefit of ocean iron fertilization by enhancing N_2O emissions, Geophys. Res. Lett., 30, 2249, doi:10.1029/2003GL018458, 24, 2003.
Kaiser, J. and Röckmann, T.: Correction of mass spectrometric isotope ratio measurements for isobaric isotopologues of O_2, CO, CO_2, N_2O and SO_2, Rapid Commun. Mass Sp., 22, 3997–4008, doi:10.1002/rcm.3821, 2008.
Kaiser, J., Brenninkmeijer, C. A. M., and Röckmann, T.: Intramolecular ^{15}N and ^{18}O fractionation in the reaction of N_2O with $O(^1D)$ and its implications for the stratospheric N_2O isotope signature, J. Geophys. Res., 107, 4214, doi:10.1029/2001JD001506, 2002.
Kaiser, J., Röckmann, T., Brenninkmeijer, C. A. M., and Crutzen, P. J.: Wavelength dependence of isotope fractionation in N_2O photolysis, Atmos. Chem. Phys., 3, 303–313, doi:10.5194/acp-3-303-2003, 2003a.
Kaiser, J., Park, S., Boering, K. A., Brenninkmeijer, C. A. M., Hilkert, A. W., and Röckmann, T.: Mass-spectrometric method for the absolute calibration of the intramolecular nitrogen isotope distribution in nitrous oxide, Anal. Bioanal. Chem., 378, 256–269, doi:10.1007/s00216-003-2233-2, 2003b.
Kaiser, J., Engel, A., Borchers, R., and Röckmann, T.: Probing stratospheric transport and chemistry with new balloon and aircraft observations of the meridional and vertical N_2O isotope distribution, Atmos. Chem. Phys., 6, 3535–3556, doi:10.5194/acp-6-3535-2006, 2006.
Kim, K. R. and Craig, H.: Nitrogen-15 and oxygen-18 characteristics of nitrous oxide: a global perspective, Science, 262, 1855–1857, 1993.
Liang, M.-C. and Yung, Y. L.: Sources of the oxygen isotopic anomaly in atmospheric N_2O, J. Geophys. Res., 112, D13307, doi:10.1029/2006JD007876, 2007.
MacFarling Meure, C., Etheridge, D., Trudinger, C., Steele, P., Langenfelds, R., van Ommen, T., Smith, A., and Elkins, J.: The law dome CO_2, CH_4 and N_2O ice core records extended to 2000 years BP, Geophys. Res. Lett., 33, L14810 doi:10.1029/2006GL026152, 2006.

ACPD
15, 19947–20011, 2015

Machida, T., Nakazawa, T., Fujii, Y., Aoki, S., and Watanabe, O.: Increase in the atmospheric nitrous oxide concentration during the last 250 years, Geophys. Res. Lett., 22, 2921–2924, 1995.
McLinden, C. A., Prather, M. J., and Johnson, M. S.: Global modelling of the isotopic analogues of N_2O: stratospheric distributions, budgets, and the ^{17}O-^{18}O mass-independent anomaly, anomaly, J. Geophys. Res., 108, 4233, doi:10.1029/2002JD002560, 2003.
Minschwaner, K., Salawitch, R. J., and McElroy, M. B.: Absorption of solar radiation by O_2: implications for O_3 and lifetimes of N_2O, $CFCl_3$, and CF_2Cl_2, J. Geophys. Res., 98, 10543–10561, 1993.
Mohn, J., Wolf, B., Toyoda, S., Lin, C- T., Liang, M-C, Brüggemann, N., Wissel, H., Steiker, A. E., Dyckmans, J., Szwec, L., Ostrom, N. E., Casciotti, K. L., Forbes, M., Giesemann, A., Well, R., Doucett, R. R., Yarnes, C. T., Ridley, A. R., Kaiser, J., and Yoshida, N.: Inter-laboratory assessment of nitrous oxide isotopomer analysis by isotope ratio mass spectrometry and laser spectroscopy: current status and perspectives, Rapid Commun. Mass Sp., 28, 1995–2007, doi:10.1002/rcm.6982, 2014.
Morgan, C. G., Allen, M., Liang, M. C., Shia, R. L., Blake, G. A., and Yung, Y. L.: Isotopic fractionation of nitrous oxide in the stratosphere: comparison between model and observations, J. Geophys. Res.-Atmos., 109, D04305, doi:10.1029/2003JD003402, 2004.
Nakazawa, T., Ishizawa, M., Higuchi, K., and Trivett, N. B. A.: Two curve fitting methods applied to CO_2 flask data, Environmetrics, 8, 197–218, 1997.
Nanbu, S. and Johnson, M. S.: Analysis of the ultraviolet absorption cross sections of six isotopically substituted nitrous oxide species using 3D wave packet propagation, J. Phys. Chem. A, 108, 8905–8913, doi:10.1021/jp048853r, 2004.
Nevison, C. D., Weiss, R. F., and Erickson III, D. J.: Global oceanic emissions of nitrous oxide, J. Geophys. Res., 100, 15809–15820, 1995.
Nevison, C. D., Mahowald, N. M., Weiss, R. F., and Prinn, R. G.: Interannual and seasonal variability in atmospheric N_2O, Global Biogeochem. Cy., 21, GB3017, doi:10.1029/2006GB002755, 2007.
Numaguti, A., Takahashi, M., Nakajima, T., and Sumi, A.: Development of CCSR/NIES Atmospheric General Circulation Model, CGER's Supercomput. Monogr. Rep., 3, 1–48, Tsukuba, Ibaraki, 1997.
Onogi, K., Tsutsui, J., Koide, H., Sakamoto, M., Kobayashi, S., Hatsushika, H. Matsumoto, T., Yamazaki, N., Kamahori, H., Takahashi, K., Kadokura, S., Wada, K., Kato, K., Oyama, R.,

ACPD
15, 19947–20011, 2015

Ose, T., Mannoji, N., and Taira, R.: The JRA-25 reanalysis, J. Meteorol. Soc. Jpn., 85, 369–432, 2007.

Park, S., Atlas, E. L., and Boering, K. A.,: Measurements of N_2O isotopologues in the stratosphere: influence of transport on the apparent enrichment factors and the isotopologue fluxes to the troposphere, J. Geophys. Res., 109, D01305, doi:10.1029/2003JD003731, 2004.

Park, S., Croteau, P., Boering, K. A., Etheridge, D. M., Ferretti, D., Fraser, P. J., Kim, K.-R., Krummel, P. B., Langenfelds, R. L., van Ommen, T. D., Steel, L. P., and Trudinger, C. M.: Trends and seasonal cycles in the isotopic composition of nitrous oxide since 1940, Nat. Geosci., 5, 261–265, doi:10.1038/ngeo1421, 2012.

Prinn, R. G., Weiss, R. F., Fraser, P. J., Simmonds, P. G., Cunnold, D. M., Alyea, F. N., O'Doherty, S., Salameh, P., Miller, B. R., Huang, J.,Wang, R. H. J., Hartley, D. E., Harth, C., Steele, L. P., Sturrock, G., Midgley, P. M., and McCulloch, A.: A history of chemically and radiatively important gases in air deduced from ALE/GAGE/AGAGE, J. Geophys. Res., 105, 17751–17792, 2000.

Rahn, T. and Wahlen, M.: A reassessment of the global isotopic budget of atmospheric nitrous oxide, Global Biogeochem. Cy., 14, 537–543, 2000.

Ravishankara, A. R., Daniel, J. S., Portmann, R. W.: Nitrous Oxide (N_2O): the dominant ozone-depleting substance emitted in the 21st century, Science, 326, 5949, 123–125, doi:10.1126/science.1176985, 2009.

Rigby, M., Manning, A. J., and Prinn, R. G.: The value of high-frequency, high-precision methane isotopologue measurements for source and sink estimation, J. Geophys. Res., 117, D12312, doi:10.1029/2011JD017384, 2012.

Röckmann, T. and Levin, I.: High-precision determination of the changing isotopic composition of atmospheric N_2O from 1990 to 2002, J. Geophys. Res., 110, D21304, doi:10.1029/2005JD006066, 2005.

Röckmann, T., Kaiser, J., and Brenninkmeijer, C. A. M.: The isotopic fingerprint of the pre-industrial and the anthropogenic N_2O source, Atmos. Chem. Phys., 3, 315–323, doi:10.5194/acp-3-315-2003, 2003.

Saikawa, E., Prinn, R. G., Dlugokencky, E., Ishijima, K., Dutton, G. S., Hall, B. D., Langenfelds, R., Tohjima, Y., Machida, T., Manizza, M., Rigby, M., O'Doherty, S., Patra, P. K., Harth, C. M., Weiss, R. F., Krummel, P. B., van der Schoot, M., Fraser, P. J., Steele, L. P., Aoki, S., Nakazawa, T., and Elkins, J. W.: Global and regional emissions estimates for N_2O, Atmos. Chem. Phys., 14, 4617–4641, doi:10.5194/acp-14-4617-2014, 2014.

ACPD
15, 19947–20011, 2015

Sander, S. P., Friedl, R. R., Golden, D. M., Kurylo, M. J., Moortgat, G. K., Wine, P. H., Ravishankara, A. R., Kolb, C. E., Molina, M. J., Finlayson-Pitts, B. J., Huie, R. E., and Orkin, V. L.: Chemical Kinetics and Photochemical Data for Use in Atmospheric Studies, Evaluation Number 15, JPL Publication 06-2, Jet Propulsion Laboratory, California Institute of 822 Technology, Pasadena, CA, 2006.

Schilt, A., Baumgartner, M., Blunier, T., Schwander, J., Spahni, R., Fischer, H., and Stocker, T. F.: Glacial–interglacial and millennial-scale variations in the atmospheric nitrous oxide concentration during the last 800,000 years, Quaternary Sci. Rev., 29, 182–192, 2010.

Schmidt, J. A., Johnson, M. S., and Schinke, R.: Isotope effects in N_2O photolysis from first principles, Atmos. Chem. Phys., 11, 8965–8975, doi:10.5194/acp-11-8965-2011, 2011.

Schmidt, M., Glatzel-Mattheier, H., Sartorius, H., Worthy, D. E., and Levin, I.: Western European N_2O emissions: a top down approach based on atmospheric observations, J. Geophys. Res., 106, 5507–5516, 2001.

Schultz, M. G., Heil, A., Hoelzemann, J. J., Spessa, A., Thonicke, K., Goldammer, J. G., Held, A. C., Pereira, J. M. C., and van het Bolscher, M.: Global wildland fire emissions from 1960 to 2000, Global Biogeochem. Cy., 22, GB2002, doi:10.1029/2007GB003031, 2008.

Sekiguchi, M. and Nakajima, T.: A *k*-distribution-based radiation code and its computational optimization for an atmospheric general circulation model, J. Quant. Spectrosc. Ra., 109, 2779–2793, 2008.

Selwyn, G. S. and Johnston, H. S.: Ultraviolet absorption spectrum of nitrous oxide as a function of temperature and isotopic substitution, J. Chem. Phys., 74, 3791–3803, doi:10.1063/1.441608, 1981.

Sowers, T., Rodebaugh, A., Yoshida, N., and Toyoda, S.: Extending records of the isotopic composition of atmospheric N_2O back to 1800 A.D. from air trapped in snow at the South Pole and the Greenland Ice Sheet Project II ice core, Global Biogeochem. Cy., 16, 1129, doi:10.1029/2002GB001911, 2002.

Sudo, K., Takahashi, M., Kurokawa, J., and Akimoto, H.: CHASER: a global chemical model of the troposphere 1. Model description, J. Geophys. Res., 107, 4339, doi:10.1029/2001JD001113, 2002.

Takigawa, M., Takahashi, M., and Akiyoshi, H.: Simulation of ozone and other chemical species using a Center for Climate System Research/National Institute for Environmental Studies atmospheric GCM with coupled stratospheric chemistry, J. Geophys. Res., 104, 14003–14018, 1999.

ACPD
15, 19947–20011, 2015

Thompson, R. L., Chevallier, F., Crotwell, A. M., Dutton, G., Langenfelds, R. L., Prinn, R. G., Weiss, R. F., Tohjima, Y., Nakazawa, T., Krummel, P. B., Steele, L. P., Fraser, P., O'Doherty, S., Ishijima, K., and Aoki, S.: Nitrous oxide emissions 1999 to 2009 from a global atmospheric inversion, Atmos. Chem. Phys., 14, 1801–1817, doi:10.5194/acp-14-1801-2014, 2014a.

Thompson, R. L., Patra, P. K., Ishijima, K., Saikawa, E., Corazza, M., Karstens, U., Wilson, C., Bergamaschi, P., Dlugokencky, E., Sweeney, C., Prinn, R. G., Weiss, R. F., O'Doherty, S., Fraser, P. J., Steele, L. P., Krummel, P. B., Saunois, M., Chipperfield, M., and Bousquet, P.: TransCom N_2O model inter-comparison – Part 1: Assessing the influence of transport and surface fluxes on tropospheric N_2O variability, Atmos. Chem. Phys., 14, 4349–4368, doi:10.5194/acp-14-4349-2014, 2014b.

Thompson, R. L., Ishijima, K., Saikawa, E., Corazza, M., Karstens, U., Patra, P. K., Bergamaschi, P., Chevallier, F., Dlugokencky, E., Prinn, R. G., Weiss, R. F., O'Doherty, S., Fraser, P. J., Steele, L. P., Krummel, P. B., Vermeulen, A., Tohjima, Y., Jordan, A., Haszpra, L., Steinbacher, M., Van der Laan, S., Aalto, T., Meinhardt, F., Popa, M. E., Moncrieff, J., and Bousquet, P.: TransCom N_2O model inter-comparison – Part 2: Atmospheric inversion estimates of N_2O emissions, Atmos. Chem. Phys., 14, 6177–6194, doi:10.5194/acp-14-6177-2014, 2014c.

Tohjima, Y., Mukai, H., Maksyutov, S., Takahashi, Y., Machida, T., Katsumoto, M., and Fujinuma, Y.: Variations in atmospheric nitrous oxide observed at Hateruma monitoring station, Chemosphere, 2, 435–443, 2000.

Toyoda, S. and Yoshida, N.: Determination of nitrogen isotopomers of nitrous oxide on a modified isotope ratio mass spectrometer, Anal. Chem., 71, 4711–4718, 1999.

Toyoda, S., Yoshida, N., Urabe, T., Nakayama, Y., Suzuki, T., Tsuji, K., Shibuya, K., Aoki, S., Nakazawa, T., Ishidoya, S., Ishijima, K., Sugawara, S., Machida, T., Hashida, G., Morimoto, S., and Honda, H.: Temporal and latitudinal distributions of stratospheric N_2O isotopomers, J. Geophys. Res., 109, D08308, doi:10.1029/2003JD004316, 2004.

Toyoda, S., Yano, M., Nishimura, S., Akiyama, H., Hayakawa, A., Koba, K., Sudo, S., Yagi, K., Makabe, A., Tobari, Y., Ogawa, N. O., Ohkouchi, N., Yamada, K., Yoshida, N.: Characterization and production and consumption processes of N_2O emitted from temperate agricultural soils determined via isotopomer ratio analysis, Global Biogeochem. Cy., 25, GB2008, doi:10.1029/2009GB003769, 2011.

Toyoda, S., Kuroki, N., Yoshida, N., Ishijima, K., Tohjima, Y., and Machida, T.: Decadal time series of tropospheric abundance of N_2O isotopomers and isotopologues in the Northern

ACPD
15, 19947–20011, 2015

Hemisphere obtained by the longterm observation at Hateruma Island, Japan., J. Geophys. Res.-Atmos., 118, 3369–3381, doi:10.1002/jgrd.50221, 2013.

Toyoda, S., Yoshida, N., and Koba, K.: Isotopocule analysis of biologically produced nitrous oxide in various environments, Mass Spectrom. Rev., doi:10.1002/mas.21459, online first, 2015.

van der Werf, G. R., Randerson, J. T., Giglio, L., Collatz, G. J., Mu, M., Kasibhatla, P. S., Morton, D. C., DeFries, R. S., Jin, Y., and van Leeuwen, T. T.: Global fire emissions and the contribution of deforestation, savanna, forest, agricultural, and peat fires (1997–2009), Atmos. Chem. Phys., 10, 11707–11735, doi:10.5194/acp-10-11707-2010, 2010.

von Hessberg, P., Kaiser, J., Enghoff, M. B., McLinden, C. A., Sorensen, S. L., Röckmann, T., and Johnson, M. S.: Ultra-violet absorption cross sections of isotopically substituted nitrous oxide species: $^{14}N^{14}NO$, $^{15}N^{14}NO$, $^{14}N^{15}NO$ and $^{15}N^{15}NO$, Atmos. Chem. Phys., 4, 1237–1253, doi:10.5194/acp-4-1237-2004, 2004.

Waechter, H., Joachim, M., Bela, T., Lukas, E., and Sigrist, M. W.: Determination of N_2O isotopomers with quantum cascade laser based absorption spectroscopy, Opt. Express, 16, 9239–9244, 2008.

Westley, M. B., Popp, B. N., and Rust, T. M.: The calibration of the intramolecular nitrogen isotope distribution in nitrous oxide measured by isotope ratio mass spectrometry, Rapid Commun. Mass Sp., 21, 391–405, doi:10.1002/rcm.2828, 2007.

ACPD
15, 19947–20011, 2015

Table 1. Stations for atmospheric N_2O mole fraction and isotopocule ratio measurements used in this study. Data from GAGE/AGAGE stations were used only for N_2O mole fraction validation.

Station	Code	Lat, Lon, Alt*	Period	Type	Components	Data source
Neumayer	NMY	71° S, 8° W, 50 m	1990–2002	Ground base	N_2O, $\delta^{15}N^{bulk}$, $\delta^{18}O$, $\delta^{15}N^{sp}$	Röckmann and Levin (2005)
Ny-Ålesund	NAL	79° N, 12° E, 40 m	1999–2002	Ground base	N_2O, $\delta^{15}N^{bulk}$, $\delta^{18}O$	Ishijima et al. (2007)
Hateruma	HAT	24° N, 124° E, 47 m	1999–pres.	Ground base	N_2O, $\delta^{15}N^{bulk}$, $\delta^{18}O$, $\delta^{15}N^{sp}$	Toyoda et al. (2013)
Cape Grim	CGO	41° S, 145° E, 21 m	1981–pres.	Ground base	N_2O, $\delta^{15}N^{bulk}$, $\delta^{18}O$, $\delta^{15}N^{sp}$	Park et al. (2012) and GAGE/AGAGE
North GRIP	NGR	75° N, 43° W, 2959 m	1952–2001	Firn site	N_2O, $\delta^{15}N^{bulk}$, $\delta^{18}O$	Ishijima et al. (2007)
Dome Fuji	DFJ	77° S, 40° E, 3810 m	1973–1999	Firn site	N_2O, $\delta^{15}N^{bulk}$, $\delta^{18}O$	Ishijima et al. (2007)
H72	H72	69° S, 41° E, 1241 m	1975–1998	Firn site	N_2O, $\delta^{15}N^{bulk}$, $\delta^{18}O$	Ishijima et al. (2007)
Mace Head	MHD	53° N, 10° W, 8 m	1987–pres.	Ground base	N_2O	GAGE/AGAGE
Cape Meares	CMO	46° N, 124° W, 30 m	1983–1989	Ground base	N_2O	GAGE
Trinidad Head	THD	41° N, 124° W, 120 m	1995–pres.	Ground base	N2O	AGAGE
Ragged Point	RPB	13° N, 59° W, 45 m	1985–pres.	Ground base	N_2O	GAGE/AGAGE
Cape Matatula	SMO	14° S, 171° W, 42 m	1985–pres.	Ground base	N_2O	GAGE/AGAGE

* a.s.l.

ACPD
15, 19947–20011, 2015

Table 2. Initial mole fractions (global mean at the surface), mean annual total emissions, and scaling factors for four N_2O isotopocules used in the simulation scenarios with small (S) and large (L) values. Each emission is obtained by multiplying the base emission by the scaling factor. The base emission consists of natural soil emissions from EDGARv2, oceanic emissions from Bouwman et al. (1995) and Jin and Gruber (2003), anthropogenic emissions from EDGARv4.2 and EDGARv4.2 FT2010, and biomass burning emissions from RETRO and GFED3.1 (see more details in Sect. 4.1.3).

Species	All	$^{14}N^{14}N^{16}O$		$^{14}N^{15}N^{16}O$		$^{15}N^{14}N^{16}O$		$^{14}N^{14}N^{18}O$		Unit	Period
Scenario	Base	S	L	S	L	S	L	S	L		
Initial value		293.7	306.6	1.079	1.126	1.079	1.126	1.073	1.121	nmol mol^{-1}	01 Jan 1984
	Scaling factor	0.85	1.10	0.0031	0.0043	0.0031	0.0043	0.0018	0.0023	–	entire
Emission	24.5	20.8	27.0	0.076	0.103	0.076	0.103	0.045	0.060	Tga^{-1} N_2O	01 Jan 1991–
	(15.6)	(13.3)	(17.2)	(0.049)	(0.066)	(0.049)	(0.066)	(0.028)	(0.037)	(Tga^{-1} N)	31 Dec 2001

ACPD
15, 19947–20011, 2015

Table 3. Observed atmospheric N_2O mole fraction, $\delta^{15}N^{bulk}$, $\delta^{18}O$ and $\delta^{15}N^{sp}$ (and their uncertainties) used to optimize the model for the north–south gradients. In the optimization calculation, only the mean interpolar differences ([NGR] – [DFJ and H72]) of the values for the period 1991–1998 were used. The hemispheric means of the optimized model for the period 1991–2001 are also shown.

Station	N_2O (nmol mol^{-1})	(Unc)	$\delta^{15}N^{bulk}$(‰)	(Unc)	$\delta^{18}O$ (‰)	(Unc)	$\delta^{15}N^{sp}$(‰)	(Unc)		Period for average
NGR	311.60	(0.07[a])	7.21	(0.03)	44.60	(0.07)	18.02	(0.05)	Measurement	1991–1998
DFJ and H72	310.30	(0.05)	7.34	(0.02)	44.66	(0.05)	18.02	(0.05)		
Difference	1.31	(0.08)	–0.12	(0.04)	–0.06	(0.08)	0.00	(0.07)		
NH	313.36	(0.16[b])	6.85	(0.08)	44.77	(0.15)	18.02	(0.13)	Model (optimized)	1991–2001
SH	312.34	(0.07)	6.95	(0.02)	44.82	(0.01)	18.01	(0.04)		
Difference	1.02	(0.18)	–0.10	(0.08)	–0.04	(0.15)	0.00	(0.14)		
Global	312.85	(0.11)	6.90	(0.04)	44.79	(0.08)	18.02	(0.08)		

[a] The uncertainties for observed data are relatively small because the standard uncertainties of the data around the digital filtered long-term trends were used as the uncertainty values.
[b] The uncertainties for the optimized model shown here are the 95 % confidence ranges estimated by Monte-Carlo simulations using the observation uncertainties.

ACPD
15, 19947–20011, 2015

Table 4. N_2O emission, $\delta^{15}N^{bulk}$, $\delta^{18}O$ and $\delta^{15}N^{sp}$ for global, Northern Hemisphere, and Southern Hemisphere total sources estimated in this and previous studies. The uncertainty associated with our ACTM estimate was at the 95 % confidence level, but that of the other estimates vary depending on the study. Top-down estimates of hemispheric $\delta^{15}N^{sp}$, based on the assumed atmospheric gradient, are in parentheses as there are no observed data for this.

Area	Period	N_2O (Tg a^{-1}N)	$\delta^{15}N^{bulk}$ (‰)	$\delta^{18}O$ (‰)	$\delta^{15}N^{sp}$ (‰)	Method	Source
GL	1991–2001	15.5 ± 0.1	−10.4 ± 0.5	31.2 ± 0.2	12.3 ± 0.9	Top-down	This study (top-down by the ACTM)[a]
	1999–2010	16.0	−6.4	35.8	8.6	Top-down	Toyoda et al. (2013)[b]
	1995	15.7 ± 0.5	−9.4 ± 3.3	27.1 ± 4.0	–	Top-down	Sowers et al. (2002)[c]
	1998	16.4	−8.4 ± 0.4	32.9 ± 0.4	11.7 ± 1.1	Top-down	Röckmann et al. (2003)[d]
	2005	17.7	−9.1 ± 0.5	32 ± 0.5	7.5 ± 3.6	Top-down	Park et al. (2012)[e]
	1991–2001	15.5	−10.1 ± 12.8	35.2 ± 15.1	12.6 ± 9.3	Bottom-up	This study (based on Toyoda et al., 2015)[f]
NH	1991–2001	8.9 ± 0.4	−14.6 ± 6.9	31.2 ± 13.6	(15.1 ± 11.9)	Top-down	This study (top-down by the ACTM)
	1999–2010	9.8	−7.9	35.3	(7.3)	Top-down	Toyoda et al. (2013)
	1991–2001	8.9	−12.1 ± 14.2	34.0 ± 15.3	12.6 ± 9.2	Bottom-up	This study (based on Toyoda et al., 2015)
SH	1991–2001	6.6 ± 0.4	−4.7 ± 9.1	31.1 ± 18.1	(8.6 ± 15.8)	Top-down	This study (top-down by the ACTM)
	1999–2010	6.2	−4.1	36.5	(10.5)	Top-down	Toyoda et al. (2013)
	1991–2001	6.6	−7.2 ± 10.8	36.9 ± 14.8	12.6 ± 9.6	Bottom-up	This study (based on Toyoda et al., 2015)

[a] Interpolar difference of $\delta^{15}N^{sp}$ is assumed to be 0.0 ± 0.05 ‰.
[b] Calculated using data from Toyoda et al. (2013).
[c] Mean and standard deviation calculated based on Table 2 therein. No $\delta^{15}N^{sp}$ measurement performed.
[d] Calculated using values in Table 2 therein and annual means of optimized model for 1998 in this study.
[e] Calculated using Table 1 and the Supplement therein.
[f] Mean and standard deviation of isotopic measurements for each source compiled by Toyoda et al. (2015) were used to calculate the mean isotopocule ratio and uncertainty, respectively, of each area's total sources.

ACPD
15, 19947–20011, 2015

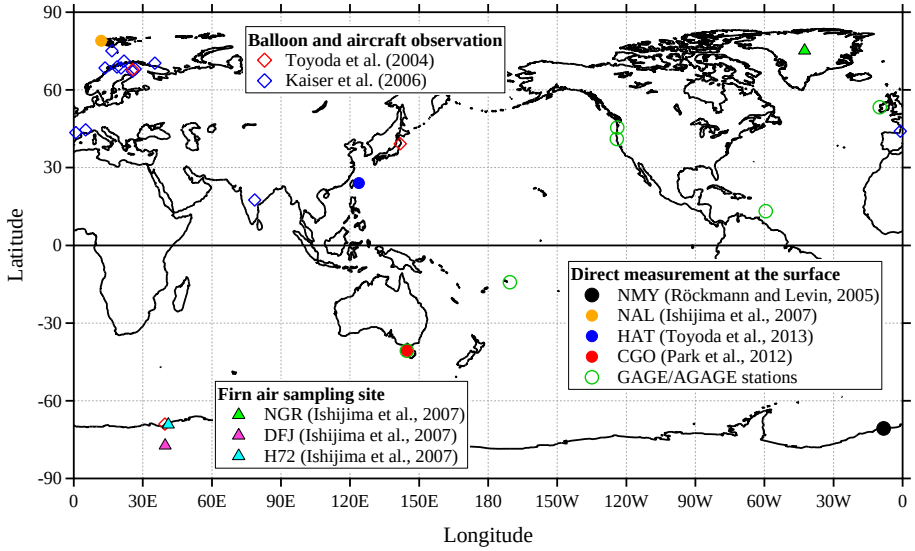

Figure 1. Locations of observation sites used in this study (and see Table 1).

ACPD
15, 19947–20011, 2015

Development of an atmospheric N_2O isotopocule model

K. Ishijima et al.

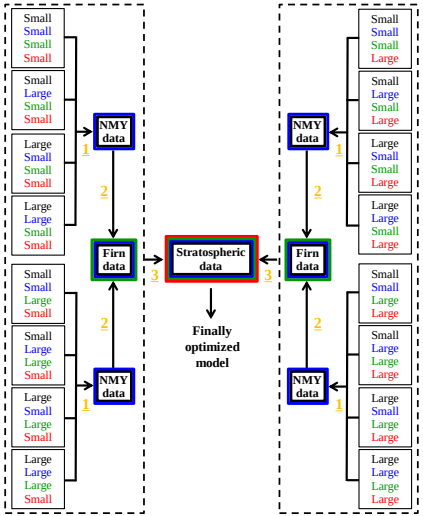

The 16 thin-line boxes indicate that 16 different simulations were performed to optimize each N_2O isotopocule. The color of "Small" or "Large" indicates which component is small or large in each scenario, as follows.

Black: Initial mole fraction (see Table 2 and Fig. S1)
Blue: Global total emission (see Table 2 and Fig. S1)
Green: NH–SH emission ratio (see Fig. S1)
Red: Photolytic fractionation
Small: Original photolysis for all isotopes,
Large: 1.5% reduced photolysis for only heavier isotopes

The colors of the thick-line boxes indicate which components were optimized by the dataset in the box. Yellow numbers indicate the following optimization steps.

1. Initial mole fraction and total emissions optimized so that the model reproduces atmospheric time series observed at NMY for the period 1990–2002 (Röckmann and Levin, 2005) as closely as possible.
2. NH–SH emission ratio optimized so that the model reproduces interpolar gradient in the atmosphere obtained from firn air analysis for the period 1991–1998 (Ishijima et al., 2007) as closely as possible.
3. Photolytic fractionation tuned so that the model reproduces apparent fractionation constant from balloon and aircraft observations in the stratosphere for the period 1987–2007 (Toyoda et al., 2004; Kaiser et al., 2006) as closely as possible.

Figure 2. Schematic representation of the model optimization procedure.

ACPD
15, 19947–20011, 2015

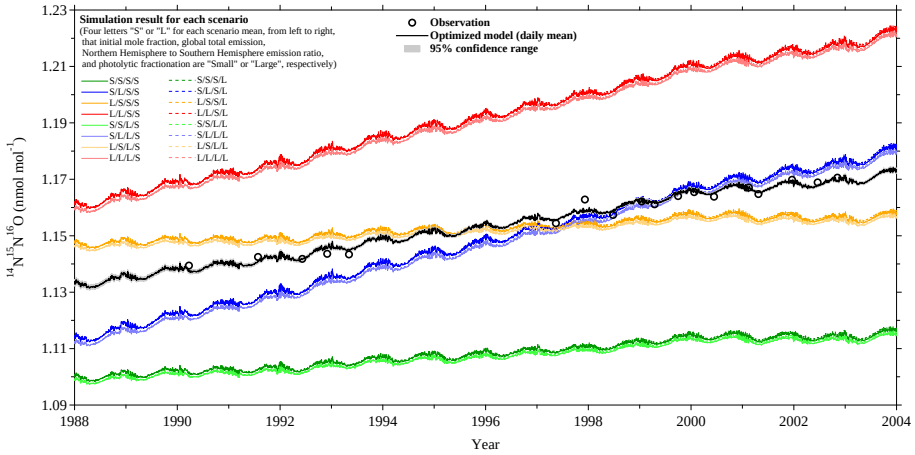

Figure 3. $^{14}N^{15}N^{16}O$ mole fraction derived from N_2O mole fraction and isotopocule ratios observed at NMY, and the optimized model results obtained by combining the 16 simulation scenarios. Simulations with small and large photolytic fractionation are almost indistinguishable (L cases show slightly higher values), especially in the first half of the period, because of their limited impact on the surface values.

ACPD
15, 19947–20011, 2015

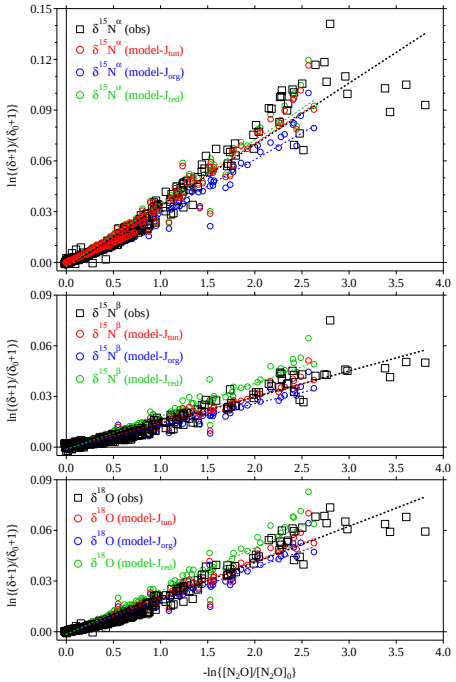

Figure 4. Rayleigh plots for $\delta^{15}N^{\alpha}$, $\delta^{15}N^{\beta}$, and $\delta^{18}O$ of stratospheric N_2O from balloon and aircraft observations (obs) and the model results (J_{tun}: with tuned photolysis rate, J_{org}: with original photolysis rate, J_{red}: with 1.5 % reduced photolysis rate for heavier isotopocules). Dashed lines represent linear-fits to the Rayleigh plots and the slopes are the apparent fractionation constant (ε). The photolysis rate for heavier isotopocules in the model is tuned so that a linear combination of the slopes of the blue and green lines is equivalent to the slope of the black line, ε_{obs} $(= f\varepsilon_{org} + (1-f)\varepsilon_{red})$. Red line represents model results from the tuned photolysis $(J_{tun} = fJ_{org} + (1-f)J_{red})$.

ACPD
15, 19947–20011, 2015

Development of an atmospheric N_2O isotopocule model

K. Ishijima et al.

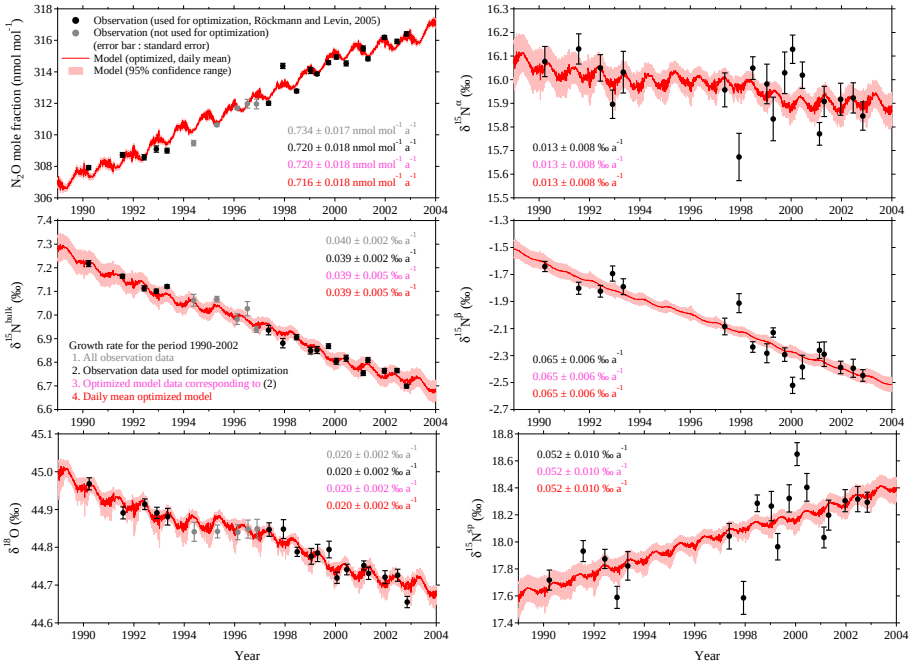

Figure 5. Atmospheric N_2O mole fraction, $\delta^{15}N^{bulk}$, $\delta^{18}O$, $\delta^{15}N^{\alpha}$, $\delta^{15}N^{\beta}$, and $\delta^{15}N^{sp}$ at NMY, Antarctica, observed (Röckmann and Levin, 2005) and simulated by the ACTM.

ACPD
15, 19947–20011, 2015

Development of an atmospheric N_2O isotopocule model

K. Ishijima et al.

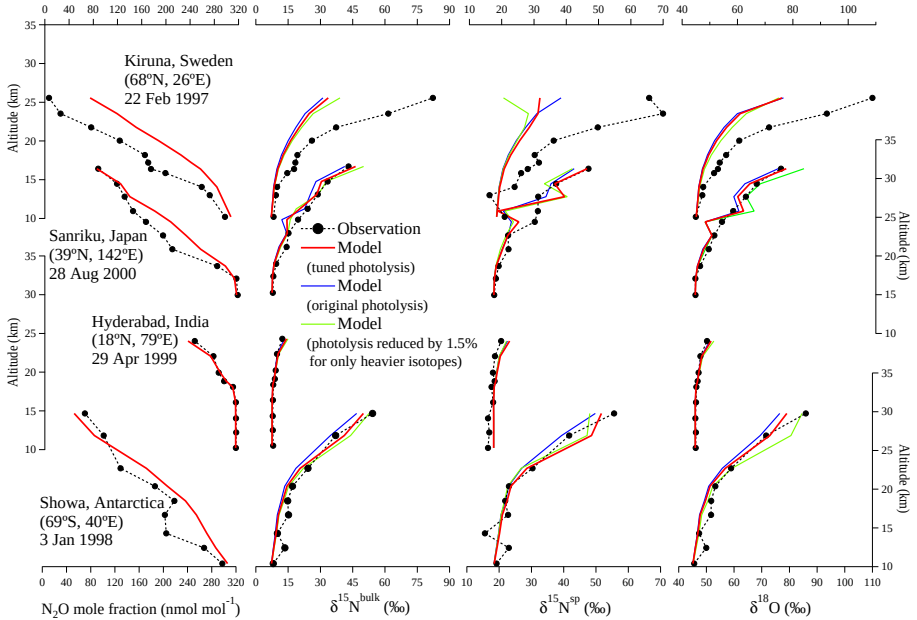

Figure 6. Vertical profiles of N_2O mole fraction, $\delta^{15}N^{bulk}$, $\delta^{18}O$, and $\delta^{15}N^{sp}$ in the stratosphere observed using balloon and simulated by the ACTM. For the isotopic results from Hyderabad, as the observed isotopocule ratios from Kaiser at al. (2006) were given relative to the tropospheric values, they were rescaled using the simulated values from NMY for the balloon observation day.

ACPD
15, 19947–20011, 2015

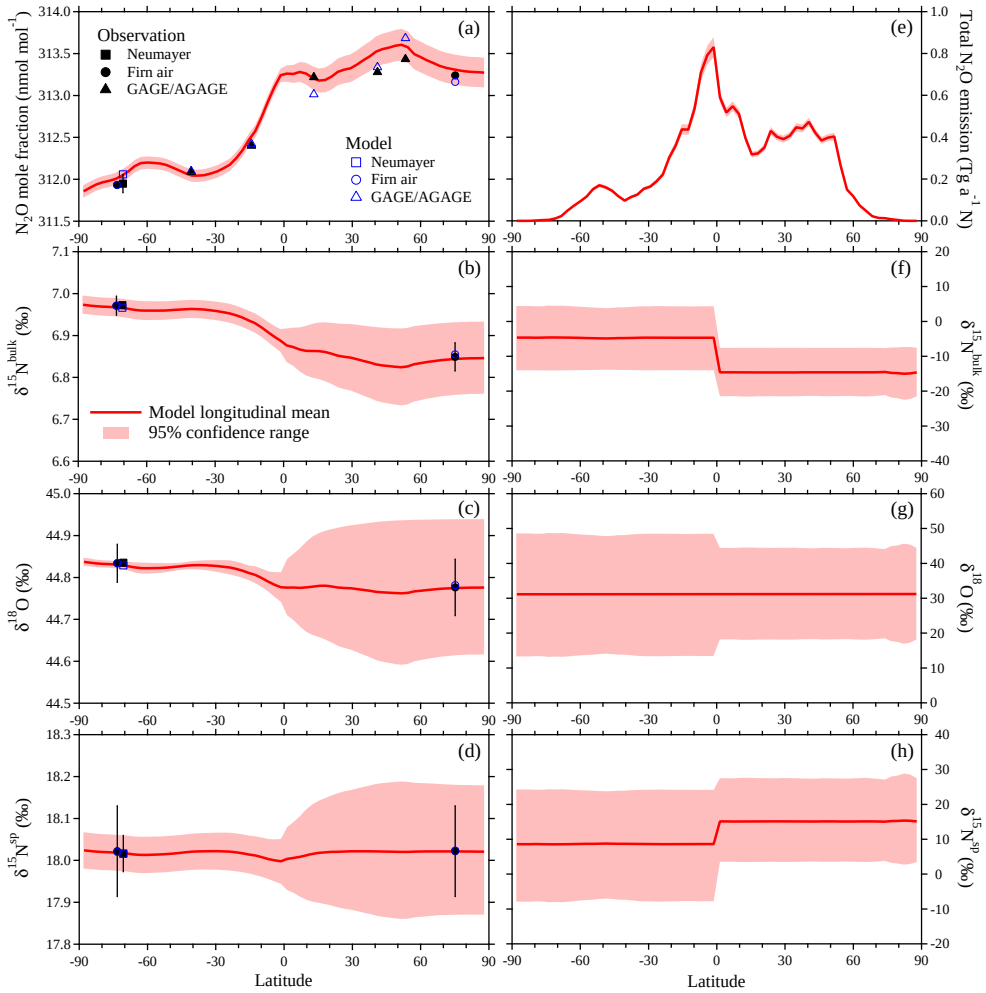

ACPD
15, 19947–20011, 2015

Development of an atmospheric N_2O isotopocule model

K. Ishijima et al.

Figure 7. Latitudinal distributions of annual means of N_2O, $\delta^{15}N^{bulk}$, $\delta^{18}O$, and $\delta^{15}N^{sp}$ in the atmosphere (**a**, **b**, **c** and **d**) and of surface sources (**e**, **f**, **g** and **h**) for the period 1991–2001 from the optimized model, and their 95 % confidence ranges. Annual means of original observation data at NMY and GAGE/AGAGE stations, which are means of the long-term trends derived using a digital-filtering technique (Nakazawa et al., 1997), are plotted, but those at the firn stations, which are means of spline-curves fitted to the data (Ishijima et al., 2007), were adjusted to the means of the optimized model results from DFJ and H72, as the standard scales differ. Error bars for the firn data represent the standard errors of the observation data around the spline-curves. The greater uncertainty in the Northern Hemisphere results from assigning a relatively large uncertainty to the interpolar difference of the observations in the optimization process, whereas the model is tightly fitted to the NMY data in the Southern Hemisphere.

ACPD
15, 19947–20011, 2015

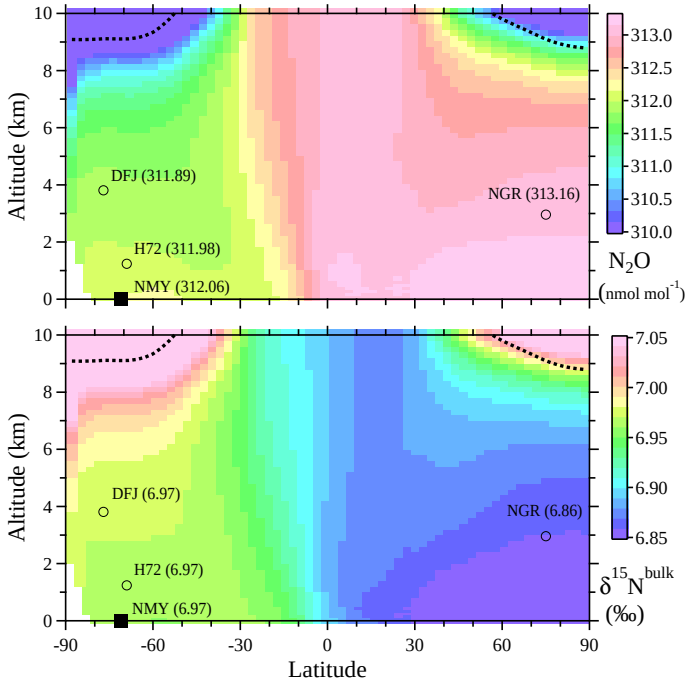

Figure 8. Annual zonal mean atmospheric N_2O mole fraction (top) and $\delta^{15}N^{bulk}$ (bottom) in the troposphere for the period 1991–2001 from the optimized model (the daily mean model outputs were simply averaged for the period). Marks represent locations of NMY, NGR, DFJ and H72 (Table 1), and black dotted lines represent tropopause height in the model as defined by a potential vorticity of 3.5 PVU and a potential temperature of 390 K. Values in parentheses represent those simulated for individual stations. $\delta^{18}O$ and $\delta^{15}N^{sp}$ also have almost the same latitudinal and vertical structures as $\delta^{15}N^{bulk}$.

ACPD
15, 19947–20011, 2015

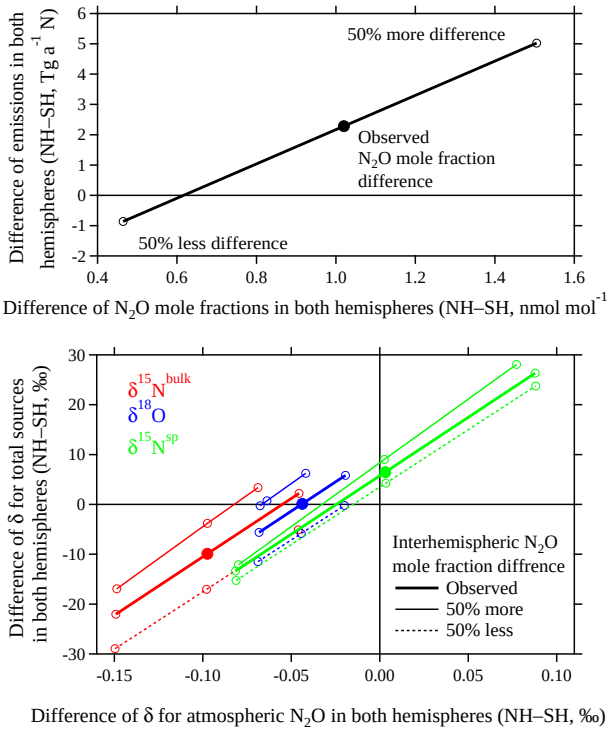

Figure 9. Sensitivities of emissions (top) and $\delta^{15}N^{bulk}$, $\delta^{18}O$, and $\delta^{15}N^{sp}$ (bottom) of hemispheric total sources to interhemispheric difference in atmospheric N_2O mole fraction, $\delta^{15}N^{bulk}$, $\delta^{18}O$, and $\delta^{15}N^{sp}$ for the period 1991–2001 in the model. The sensitivities were estimated by optimizing the model against the 50 % reduced or increased observed interhemispheric difference in atmospheric N_2O mole fraction and isotopic delta values (Table 3), but without changing the data at NMY. Therefore, the estimated global total emissions were similar in all cases ($15.45 \pm 0.03\,Tg\,a^{-1}\,N$).

ACPD
15, 19947–20011, 2015

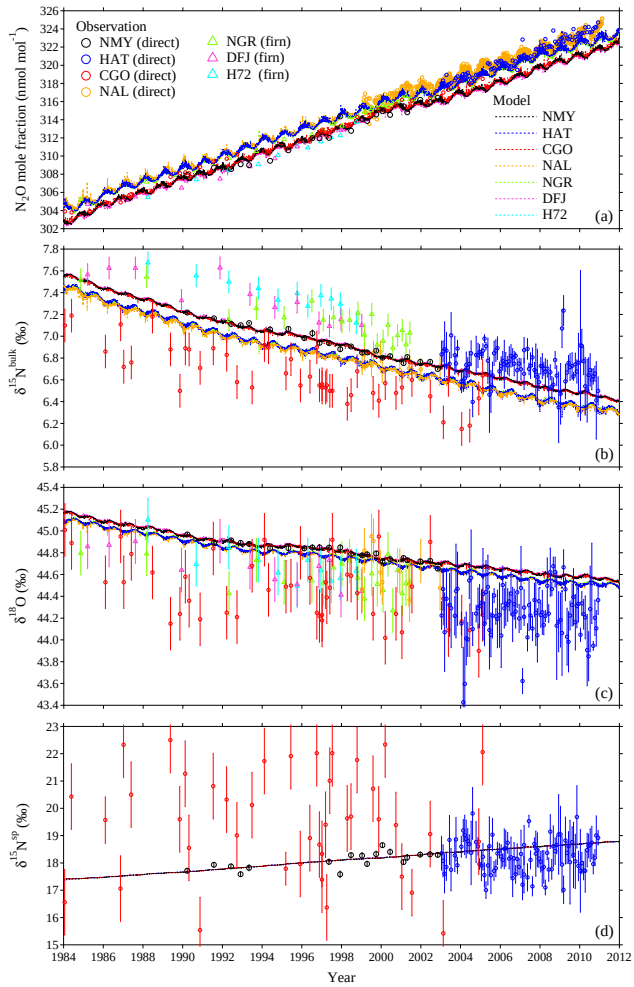

20010

ACPD
15, 19947–20011, 2015

Development of an atmospheric N_2O isotopocule model

K. Ishijima et al.

Figure 10. Atmospheric N_2O mole fraction **(a)**, $\delta^{15}N^{bulk}$ **(b)**, $\delta^{18}O$ **(c)**, and $\delta^{15}N^{sp}$ **(d)** obtained from ground-based observations, firn air analysis (see Fig. 1 and Table 1 for details of the stations), and the optimized model (daily mean output). The standard scale for each observation was not adjusted and each is plotted at the original scale.

ACPD
15, 19947–20011, 2015